

Sedimentation in the ephemeral landslide dammed paleolake in Indo-Burmese Range: Late Pleistocene-Holocene climatic variability and surface processes coupling

Arindom Gogoi ^{a,b}, Prabha Pandey ^{a,b,*}, Anand K. Pandey ^{a,b}

^a CSIR - National Geophysical Research Institute, Hyderabad 500007, India

^b Academy of Scientific and Innovative Research (AcSIR), Ghaziabad 201002, India

ARTICLE INFO

Editor: Dr. P. Srivastava

Keywords:

OSL dating
Fluvial sediment
Holocene
Landslide Lake
Indo-Burmese Range
Indian Summer Monsoon

ABSTRACT

The Late Pleistocene-Holocene marks a sharp transition in climate perturbation affecting landform patterns and depositional sequence in tectonically active regions. We investigate the fluvial landforms and Holocene fluvial-lacustrine sedimentary sequences in an ephemeral landslide-dammed intra-montane paleolake, which acts as an archive for reconstructing extreme events driven surface processes and paleo-climatic history along the Daili-Imphal River in the Indo-Burmese Range. The effect of climate-tectonic coupling on surface processes is explored through quantitative geomorphologic analysis of the landscape and sedimentological proxies, including grain size and shape analysis, geochemistry, and optically stimulated luminescence (OSL) dating of the lacustrine sequence. This analysis helps constrain the climatically sensitive hydrodynamics during the Late Pleistocene-Holocene period. The lack of grain size, geochemical variations in the sediment column, and geochemical affinity with the substrate, the Disang Shale Formation, point towards the dominance of erosion from a proximal sediment source. We argue that the pre-Holocene Bølling-Allerød (12–12.9 ka) climatic extreme caused excessive mass wasting, which blocked the Daili-Imphal River and formed a paleolake, paradoxically resulting in a low sedimentation rate during the early Holocene. The sedimentation rate increased during the Mid-Late Holocene due to local climatic optima. This unique setup highlights the role of local climatic fluctuations on the ephemeral growth of geomorphic and sedimentary archives.

1. Introduction

The Indian Summer Monsoon (ISM) experienced short-lived climate fluctuation driven by decadal to centennial atmospheric fluctuations and decreasing millennial-scale insolation during the Late Pleistocene-Holocene (Petit et al., 1999; Breitenbach, 2009). Riverine and paleolake stratigraphic records from this period have been widely used to reconstruct paleo-climatic fluctuations, paleo-earthquakes, landslides, and landscape evolution (Dethier and Reneau, 1996; Bookhagen et al., 2001; Kale, 2007; Pandey et al., 2009; Pandey et al., 2014; Misra et al., 2019; Bohra et al., 2024). In active mountainous regions, channels are often blocked by earthquakes or rainfall-triggered landslides, forming ephemeral lakes that accumulate sediment until they are breached by another triggering event (Hewitt, 1982; Costa and Schuster, 1987; Weidinger, 1998; Wang et al., 2019; Guo et al., 2020). Such variations in sedimentation may create geomorphic markers that preserve critical

information about surface processes. River terraces are important geomorphic markers that serve as temporary sediment storage along valleys and are sensitive to tectonic activity and climatic fluctuations (Trauth and Strecker, 1999; Bookhagen et al., 2001). Grain size distribution within these sedimentary records provides insights into sediment transport mechanisms and depositional environments, while sediment geochemistry reflects chemical maturity, paleoclimatic conditions, and provenance (Allen, 1985). Additionally, minerals such as quartz and feldspar are commonly used to constrain the timing of deposition (Murray et al., 2021).

The variations in the ISM are reflected in the riverine and lacustrine sedimentary records of the Indian subcontinent as phases of erosion, variation in sediment supply, and sediment aggradation (Kale, 2007; Misra et al., 2019; Bohra et al., 2024). These studies reveal that ISM intensity peaked between 9 and 5 ka and gradually declined after 4 ka with increased aridity. The climatic variations during the Late

* Corresponding author at: CSIR - National Geophysical Research Institute, Hyderabad 500007, India.

E-mail addresses: ppandey.ngri@csir.res.in (P. Pandey), akpandey.ngri@csir.res.in (A.K. Pandey).

Pleistocene to the Late Holocene are well preserved in the speleothem records from the Shillong Plateau and pollen records from lakes and swamps in Northeast India. Speleothem data indicate that the ISM intensified around 33–32 ka, marking the onset of the Last Glacial Maximum (LGM), experienced a sharp strengthening during the Bølling-Allerød period (12–12.9 ka), and remained strong throughout the early Holocene (10–6 ka) (Breitenbach, 2009; Berkelhammer et al., 2012; Dutt et al., 2015; Sengupta et al., 2025). In contrast, pollen records indicate a consistently warm and humid climate in Northeast India during the Holocene (Misra et al., 2019).

An isolated catchment along the Daili-Impal River, draining over a uniform litho-tectonic unit (Disang Shale of Eocene), adjacent to an active strike-slip fault in the Indo-Burmese Range, preserves well-developed river terraces with a > 2 m thick fluvio-lacustrine deposit (Figs. 1b, 2a). This deposit presents a conspicuous case for exploring the effects of climatic and tectonic coupling on surface processes and sediment supply in an evolving landscape. In the present study, we employed quantitative geomorphic constraints, grain-size and grain-texture analysis, geochemical characterization, and OSL dating to investigate the river blockade and the subsequent formation of a paleolake in a distinct erosional-depositional setting during Late Pleistocene-Holocene climatic fluctuations. The study particularly focuses on the sedimentation history of the landslide-dammed paleolake in NE India, with special emphasis on changing depositional patterns as indicators of

climatic variability and associated geomorphic processes.

2. Geological and geomorphic setting

The seismically active Indo-Burmese Range (IBR) is a westward-propagating accretionary wedge developed due to the hyper-oblique convergence of the Indian plate beneath the Burmese plate (Nandy, 1986; Acharyya, 2010). Seismicity in the IBR progressively becomes deeper towards the east due to the reactivation of pre-existing faults, and the strike-slip shearing dominates the shallow deformation during the Quaternary (Panda et al., 2020). Geodetic observations suggest that ~36 mm/year India-Sunda relative motion is partitioned into ~18–20 mm/year at the Sagaing Fault, ~16 mm/year at the Churachandpur-Mao Fault (CMF), and ~7 mm/year arc-normal motion on the Blind Mega Thrust (BMT) in Bangladesh (Gahalaut et al., 2013; Panda et al., 2020). The IBR is subdivided into three tectonic units: Core, Inner, and Outer wedges, from east to west. The Kabaw Fault zone separates the Central Myanmar Basin (CMB) from the core (Fig. 1b). The Core consists of Cretaceous-Tertiary imbricate metamorphic rocks, dismembered ophiolites covered with Eocene-Oligocene flysch sediments of the Disang Group and Barail Group (Fig. 1b, c). The CMF segments the highly deformed Disang and Barail Groups in the Manipur Hills, separating the Inner wedge from the Core (Evans, 1932; Nandy, 1986; Acharyya, 2010). The Neogene shallow marine-fluvial sedimentary rocks of the

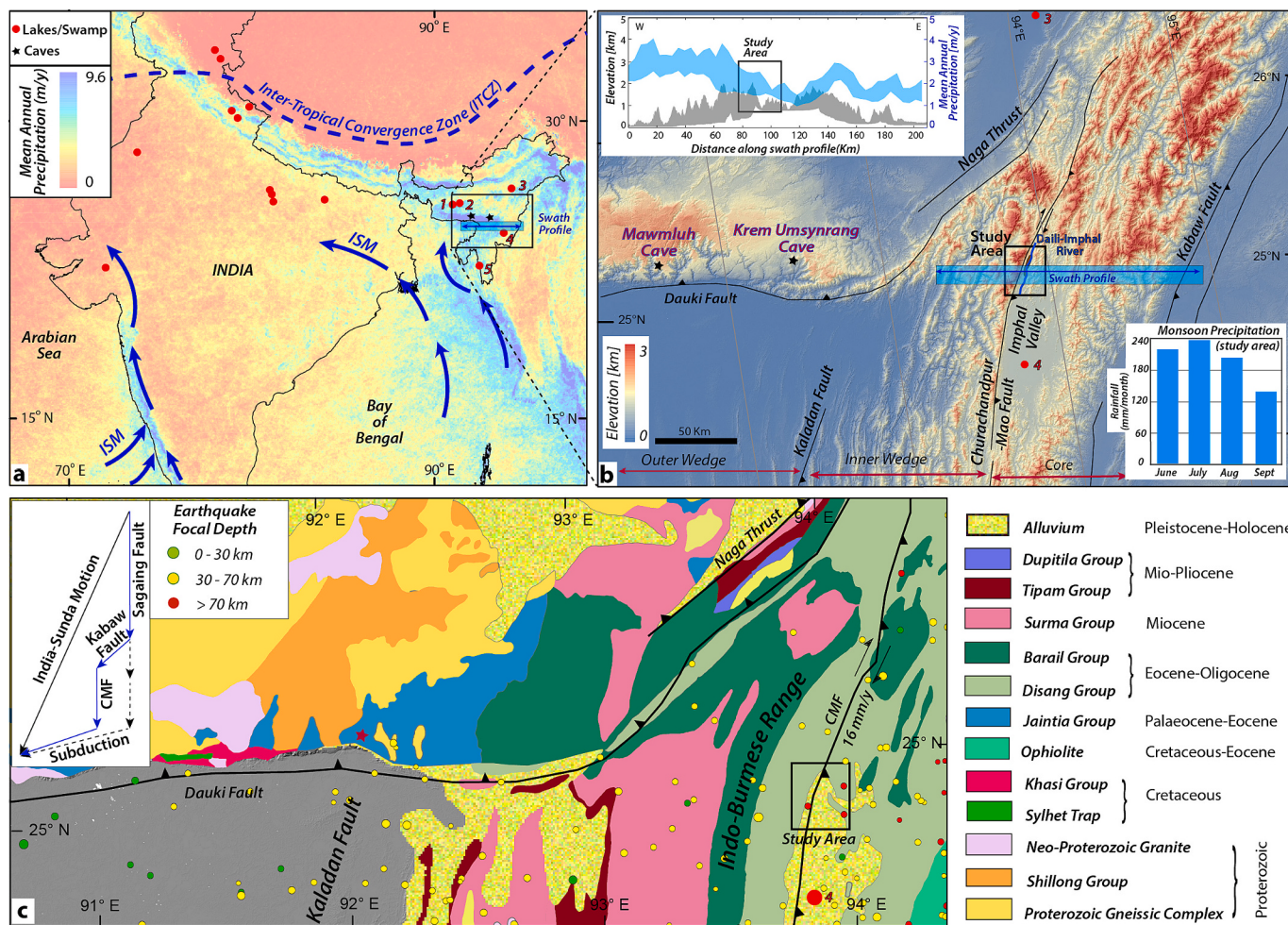


Fig. 1. (a) TRMM annual averaged for 12-year rainfall map of the Indian subcontinent, with the blue arrow showing the pathways of the Indian Summer Monsoon (ISM); and red dots and black stars mark the locations of lakes/swamps and caves, respectively; (b) Topographic map of the Indo-Burmese Range (IBR) overlaid with major structural features. Inset swath profiles depict topography and rainfall variability across the IBR, and the bar graph shows precipitation intensity during the monsoon period. (c) The geological map of the IBR (modified from the Geological Survey of India) is overlaid with earthquake distributions (colored dots). (For interpretation of the references to colour in this figure legend, the reader is referred to the web version of this article.)



Fig. 2. (a) Google Earth image of the Daili-Imphal River region overlaid with Quaternary fluvio-lacustrine sediments (blue area), and debris fan (orange area). (b) The Disang Shale forms the substrate of the Daili-Imphal catchment. (c) Well-preserved fluvio-lacustrine sediment is exposed along the Daili-Imphal River. (For interpretation of the references to colour in this figure legend, the reader is referred to the web version of this article.)

Surma and Tipam Group constitute the Outer wedge in the footwall of the Kaladan fault (Mitra, 1971). Pleistocene-Holocene alluvium overlies the Disang Shale bedrock in the core region of the Daili-Imphal River valley (Fig. 1c), where the study area is located. The N-S trending a dextral strike-slip CMF accommodates 47 % of India-Sunda plate motion through aseismic creep (Gahalaut et al., 2013), and has a significant influence on the local geomorphology of the Daili-Imphal River catchment in the study area.

The Daili-Imphal catchment ($\sim 220 \text{ km}^2$) receives a mean annual precipitation of $\sim 1.7 \text{ m/year}$, with peak monsoonal rainfall of $\sim 240 \text{ mm/month}$ between June and September (Fig. 1a), as observed in Tropical Rainfall Measuring Mission (TRMM) datasets (Bookhagen and Burbank, 2010). The precipitation pattern suggests the Daili-Imphal valley is parched compared to surrounding areas (Fig. 1b). The Daili-Imphal River drains flow over the Disang Shale substrate and debouches to the Imphal valley through a narrow gorge incised into the debris fans (Figs. 1c and 2a, b). The wider western slope of the valley has several sub-catchments with distinct erosional and aggradational landforms separated by the Churachandpur-Mao Fault (CMF). In contrast, the smaller eastern slope lacks such features (Fig. 2a). The erosional landforms of the upper slopes provide debris to the aggradational fans in the gentler downslope region of the western flank. Upstream of the valley exit, the Daili-Imphal river meanders through a broad floodplain consisting of fluvio-lacustrine deposits that overlay the Disang Shale bedrock with a distinct strandline along the western margin of the valley (Fig. 2a, c). These lacustrine deposits are well preserved in the Kalapahar area (Fig. 2c), which is exposed as a terrace section due to channel incision. The association of valley exit through multiple debris fans and the upstream fluvio-lacustrine succession (Fig. 2). These suggest episodes of mass-wasting, channel-valley blockade, and deposition in the dammed river, which acts as a repository of tectonic-climatic perturbations and sedimentation over a geological period.

3. Materials and methods

We used geomorphic, sedimentological, and geochemical proxies to understand tectonic-climatic interaction, and details of the methods are presented in the following section.

3.1. Geomorphic analysis, terrace mapping, and sampling

We used Google Earth imagery and Advanced Land Observing Satellite (ALOS) PALSAR 12.5 m DEM to map the study region in a GIS platform. We used TopoToolbox (Schwanghart and Scherler, 2014) for quantitative geomorphic analysis, including delineating the river profile, terrace-debris fan mapping, and calculating the normalized channel steepness index (k_{sn}). The Geophysical Relief (G_R) and volumetric estimation for erosion and depositional budgeting were estimated in ArcGIS for the Daili-Imphal Valley to understand the role of CMF in slope evolution.

The Erosion potential (E) of the bedrock channel can be expressed as a power law function of drainage area (A) and channel slope (S) (Whipple and Tucker, 1999; Wobus et al., 2006), as expressed in Eq. 1.

$$E = KA^m S^n \quad (1)$$

The K is called the erodibility coefficient, m is the area exponent, and n is the slope exponent. For the steady state $\left(\frac{dz}{dt} = \text{Uplift}(U) - \text{Erosion}(E) = 0 \right)$ bedrock river profile evolution equation can be written as Eq. 2:

$$k_s = A^{\frac{m}{n}} S \quad (2)$$

where the k_s is the channel steepness index, and m/n is the concavity of the channel. Since, k_s and concavity (m/n) are highly correlated, slope is normalized for upstream drainage area by replacing the concavity (m/n)

value with a reference concavity θ_{ref} producing normalized steepness index (k_{sn}), which is used as a proxy for erosion potential within a uniform climatic and tectonic setting and can be compared regardless the size of the drainage area (Whipple and Tucker, 1999; Wobus et al., 2006). The k_{sn} is calculated using Eq. 3

$$k_{sn} = A^{\theta_{ref}} S \quad 3$$

We used the “mnoptim” function of Topotoolbox, which applies a Bayesian Optimization technique to determine the optimum value of reference concavity (θ_{ref}). For the study area, the calculated θ_{ref} is 0.45 (SM Fig. 1), which was used to calculate k_{sn} in the present study.

The Geophysical Relief (G_R) represents the minimum thickness of material removed or accumulated by erosion or deposition (Small and Anderson, 1998). It is obtained by extrapolating an elevation surface from the drainage divide to its corresponding river bed in a GIS platform. The volumetric estimation was done by summing the geophysical relief over the catchment area to estimate the eroded volume of the catchments and the debris fans using Eq. 4.

$$\text{Volume (m}^3\text{)} = \sum (\text{DEM pixel resolution (12.5 m} \times 12.5 \text{ m}) \times G_R) \quad 4$$

We identified well-developed terraces (T1 and T2) and mapped the confined floodplain deposits (Fig. 2a). Using a handheld GPS, we recorded the sample locations and measured the terrace heights. We cleared the vertical T2 terrace section and collected 14 fine-grained sediment samples at 10 cm intervals for grain size and geochemical analysis. We also collected four OSL samples in concealed aluminum pipes at depths of 50 cm, 90 cm, 140 cm, and 170 cm from the top of the T2 terrace to get temporal constraints on the sediment aggradation rates. Sampling from the T1 terrace was unsuitable for OSL dating due to the clast-supported, coarse-grained sediments.

3.2. Grain size study

Sediment grain size properties indicate energy levels, transport processes, and sediment mixing (Folk and Ward, 1957). The grain size analysis of fine-grained sediments was carried out on a Malvern Hydro 2000MU Laser Particle Size Analyzer (LPSA), which measures the diffraction pattern of the laser light in the solution caused by suspended particles, where particle size is inversely proportional to the diffraction angle (Beuselinck et al., 1998). Approximately 7–10 g of oven-dried samples were taken after coning and quartering and were treated with 30–40 ml of H_2O_2 to remove all the organic matter, as organic matter can cause coarse skew in the grain size distribution pattern (Allen and Thornley, 2004). The samples were further treated with 1 N HCl to remove carbonate matter from the sediments. The distilled water (refractive index: 1.33) was used as the liquid dispersant, and the samples were added until the obscuration range reached 10–20 %. The measurements were carried out, and the results were reported as volumetric percentages. Sample statistics were calculated using the Folk and Ward (1957) method in the GRADISTAT platform (Blott and Pye, 2001).

The morphological properties of sediment grains, such as form, degree of roundness, and surface texture, provide valuable information

about weathering, erosion, transportation, deposition, and geomorphological evolution (Barrett, 1980; Mazzullo and Magenheimer, 1987; Gresina et al., 2023). The clay fraction was removed from the sediment aggregate by rinsing with distilled water, and the granular fraction was mounted on thin sections using Araldite epoxy. The grain morphology was examined using a Hitachi S-340 N Scanning Electron Microscope (SEM) at CSIR-NGRI, Hyderabad. Backscattered electron (BSE) images were taken at 15-kV electron beam accelerating voltage, 8.2 mm working distance in VP-SEM mode. The BSE images of coarser grain fractions were analyzed in ImageJ software to calculate the particle shape and size parameters such as Circularity (C), Elongation Ratio (E), Roundness (R), and Solidity (S) using Eqs. 5–8 (Cox, 1927; Powers, 1953; Gresina et al., 2023; SM Table 1).

$$\text{Circularity (C)} = \frac{4\pi(\text{Area})}{\text{Perimeter}^2} \quad 5$$

$$\text{Elongation Ratio (E)} = \frac{\text{Minor axis}}{\text{Major axis}} \quad 6$$

$$\text{Roundness (R)} = \frac{4(\text{Area})}{\pi(\text{Major axis})^2} \quad 7$$

$$\text{Solidity (S)} = \frac{\text{Area}}{\text{Convex Area}} \quad 8$$

The circularity index is the ratio of the area of the grain to the area of a circle with the same perimeter (Cox, 1927) and is a two-dimensional equivalent of true sphericity proposed by Wadell (1932). Elongation is the ratio of the Minor axis to the Major axis, and its value ranges between 0 and 1. Roundness is the measure of the angularity of the grain, and the solidity parameter characterises the smoothness of the grain surface.

3.3. Geochemical analysis

Sediment chemistry helps in understanding their provenance, diagenetic history, and compositional maturity (Allen, 1985). For geochemical analysis, oven-dried samples were powdered, and pellets were prepared using a hydraulic press for each sample. The Loss-on-Ignition (LOI) was also measured. Analysis for major oxides (SiO_2 , Al_2O_3 , Fe_2O_3 , MgO , CaO , Na_2O , K_2O , TiO_2 , P_2O_5 , MnO) was carried out in PANalytical Axios mAX wavelength dispersive-XRF at CSIR-NGRI, Hyderabad. Chemical Index of Alteration (CIA) (Nesbitt and Young, 1982), Index of Compositional Variability (ICV) (Cox et al., 1995), Ti/Al, and Si/Al were calculated to understand sediment chemistry changes in response to climatic variability. We calculated the CIA and ICV indices using Eqs. 9 and 10 by applying corrections to exclude CaO from the carbonate and apatite fractions, as McLennan (1993) outlined. The CaO^* represents CaO from silicate fractions only (Fedo et al., 1995) and is obtained by $CaO^* = CaO - 3.33 P_2O_5$; if $CaO^* > Na_2O$, then $CaO^* = Na_2O$; if $CaO^* < Na_2O$, then $CaO^* = CaO^*$, where concentrations are in molar units.

$$CIA = [Al_2O_3 / (Al_2O_3 + CaO^* + Na_2O + K_2O)] \times 100, \quad 9$$

Table 1

The Luminescence dates of the sediment samples in the lake sediment column (Location Lat: 25°07'30.6" N, Lon: 93°57'57.4" E, Elevation: 994 m), datum year is 1950.

Sample Id	Depth (m)	U (ppm)	Th (ppm)	K ₂ O (%)	Moisture Content (%)	De (Gy)	OD (%)	Cosmic rate (mGy/yr)	Dose Rate (mGy/yr)	CAM Age (year)	Sedimentation rate (cm/ka)
OSL-01 (n = 16)	0.5	1.98	16.2	2.12	8.55	8.88 ± 0.57	21 ± 4	0.22 ± 0.02	3.31 ± 0.2	2615 ± 235	30
OSL-02 (n = 22)	0.9	1.58	16.48	2.02	8.42	12.57 ± 0.75	23 ± 4	0.19 ± 0.02	3.13 ± 0.19	3940 ± 340	33
OSL-03 (n = 23)	1.4	1.61	16.32	1.89	10.84	15.94 ± 0.55	7 ± 2	0.19 ± 0.02	2.9 ± 0.17	5430 ± 375	5
OSL-04 (n = 22)	1.7	1.85	16.68	1.87	12.44	33.31 ± 2.01	23 ± 4	0.19 ± 0.02	2.9 ± 0.17	11,405 ± 975	

$$\text{ICV} = (\text{Fe}_2\text{O}_3 + \text{K}_2\text{O} + \text{Na}_2\text{O} + \text{CaO}^* + \text{MgO} + \text{MnO})/\text{Al}_2\text{O}_3 \quad (10)$$

3.4. OSL dating

The study area primarily consists of sedimentary rock, and we expect a high concentration of quartz grains in the sediments. For the OSL dating of quartz grains, the collected samples were treated with 1 N HCl to remove the carbonates, followed by 40 % H_2O_2 to remove the organic matter from the samples (Aitken, 1998). Samples were further treated with 40 % HF for 80 min to remove the outer layer ($\sim 20 \mu\text{m}$) of the quartz grains to minimize the effect of alpha dose. The oven-dried treated samples were sieved to retain a grain size of 90–150 μm , and measurements of luminescence signals for equivalent dose were carried out in the Riso DA 20 TL/OSL reader at CSIR-NGRI, Hyderabad. The quartz purity test of each sample suggests OSL signals are appropriate for obtaining the date. Preheat test was performed for each sample at temperatures from 160 °C to 280 °C to optimize the preheat temperature. The samples were analyzed using the Double-SAR (Single-Aliquot Regenerative-dose) protocol to minimize the contribution of feldspar mineral (Murray et al., 2021). The concentrations of uranium (U), thorium (Th), and potassium (K) were determined using WD-XRF, and moisture content was measured for dose rate calculations. We used the LDAC (v1.0) platform (Liang and Forman, 2019) for age determination. Additionally, a Monte Carlo simulation with 5000 iterations was performed for each analysis to enhance the accuracy of the results (Murray et al., 2021).

4. Results

The Daili-Imphal valley section has been analyzed for landscape growth, weathering, depositional environment of lacustrine sediments, and age of deposition.

4.1. Transient landscape

The south-flowing Daili-Imphal valley shows distinct landscape variations, which are analyzed through transient landscape characterization and sediment budgeting. The narrow eastern slopes have steep bedrock topography with no aggradational features, while the western slopes exhibit both erosional and aggradational landforms across the CMF (Figs. 2a, 3a). To assess the region's erosional potential and source of sediment that produced aggradational landforms, k_{sn} map of the Daili-Imphal valley is generated (Fig. 3a inset) using a reference concavity of 0.45 (SM Fig. 1). It is observed that the k_{sn} values of the well-developed western slope are significantly higher compared to those of smaller eastern slopes (Fig. 3a, inset). The k_{sn} shows characteristic lower values ranging from 0 to 100 $\text{m}^{0.9}$ in the floodplain with valley floor deposits. The k_{sn} increases to 150 $\text{m}^{0.9}$ in the Piedmont area until the CMF (Fig. 3a), and the k_{sn} rises sharply over 150 $\text{m}^{0.9}$ into a predominantly erosional hill slope zone upstream of the CMF (Fig. 3a). The k_{sn} distribution clearly defines the variation in stream power responsible for distinct erosional and depositional localization across the CMF (Fig. 3a).

The region experienced prominent landscape growth with the

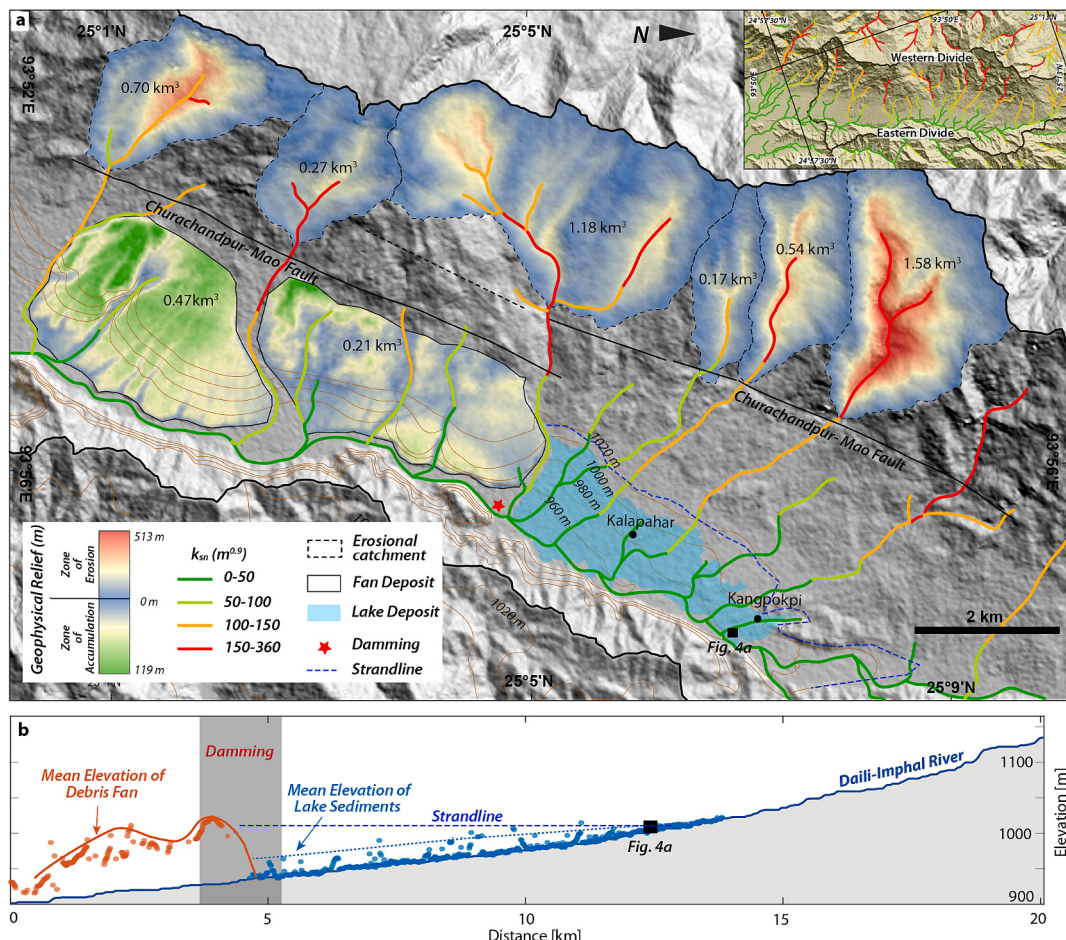


Fig. 3. (a) Inset- high k_{sn} values (red) mark the areas of high erosion in the Daili-Imphal catchment region. Geophysical relief map showing the erosional catchments and sediment aggradation in the debris fans overlaid with the k_{sn} map. (b) The longitudinal profile of the Daili-Imphal River shows the mean elevation of the lacustrine deposit, the lake strandline, and the location of the river dam by debris fan. (For interpretation of the references to colour in this figure legend, the reader is referred to the web version of this article.)

development of hills and valleys, which keeps the catchment in a transient state. We estimated the erosional volume using Geophysical Relief (G_R), which provides a minimum estimate (Small and Anderson, 1998). The entire Daili-Imphal valley experienced erosion of $>62 \text{ km}^3$ of sediments, mainly from the western slopes, since inception of the valley (SM Fig. 2). However, to understand the differential erosion and aggradation across the CMF, we estimated the G_R for the smaller catchments on the western slope (Fig. 3a; SM Fig. 2). The volumetric estimate indicates that at least 4.44 km^3 of sediments were eroded from catchments upstream of the CMF zone, off which $\sim 0.68 \text{ km}^3$ are preserved in the debris fans (Fig. 3a) represent $\sim 15\%$ of the total eroded sediment volume.

The valley floor is over 500 m wide with a distinct strandline on the western slope coinciding with the 1020 m contour (Fig. 3a). It is primarily occupied by flat to gently inclined Quaternary sediment fill derived from the western slopes (Fig. 3a). Mapping of the river's long profile, piedmont fans, and the valley-floor deposits clearly shows that the mean elevation of the preserved debris fans is higher than the strandline. In contrast, the mean elevation of the valley floor deposits decreases downstream, following the river profile and lying well below the strandline (Fig. 3b). The dissected valley floor deposits were highly incised and poorly preserved as patches towards the debris fan, where the Daili-Imphal river debouches. However, in the upstream section, well-preserved fine-grained fluvio-lacustrine deposits constitute the T2 terrace (Fig. 4a), which has been sampled for a detailed study. Field investigation along the Daili-Imphal River shows that the T1 and T2 terraces are aggradational terraces developed on the bedrock strath (Fig. 4a). The T2 Terrace is 4.6 m in height from the river bed and is composed of massive deposits of fine-grained sediments, mostly silt-clay-sand in the top $\sim 2 \text{ m}$ over a basal gravel layer (Fig. 4b). The younger Terrace T1 is 1.7 m in height from the river bed and mainly

comprises boulder, cobble, and gravel-sized clast-supported conglomeratic sediments (Fig. 4a).

4.2. Sedimentological characterization of the sediment column

Streambed sediment grain size provides critical insights into stream behavior, including energy conditions, transport processes, and sediment mixing (Folk and Ward, 1957; Allen, 1985). The grain size analysis of the T2 sediment column revealed no significant variations (Fig. 5). The sediments primarily consist of 50 % silt, $\sim 30\%$ fine to medium sand, and $\sim 20\%$ clay, exhibiting unimodal to bimodal distributions skewed towards finer grain sizes (Fig. 5; SM Fig. 3). The median grain size (D_{50}) represents the particle size at which 50 % of the sediment sample is finer and indicates the depositional energy conditions. We have observed D_{50} falls within the medium-silt range, with slight variations (Fig. 5), suggesting a stable, low-energy depositional environment (Boggs, 2009). Skewness values range from 0.1 to 0.5, indicating fine-skewed (Fk) to strongly fine-skewed (SFk) distributions (Fig. 5). This trend suggests a predominance of finer grains, implying a limited and steady sediment supply with minimal influx of coarser material. The kurtosis values (0.8–1.2) indicate a predominantly mesokurtic (Mk) distribution, indicative of poor sediment mixing and minimal transport (Folk and Ward, 1957). Sorting values, which measure grain-size variability, range from 2.1 to 2.6, classifying the sediment as very poorly sorted (VPS) within the silt fraction (Fig. 5). This poor sorting of silt-dominated sediments within the Daili-Imphal catchment points towards short transport and deposition in a calm lacustrine environment lacking dynamic sediment input, primarily originating from the fine-grained Disang Shale Formation. Additionally, the absence of bedding and laminae indicates a lack of seasonal variation in sediment input,

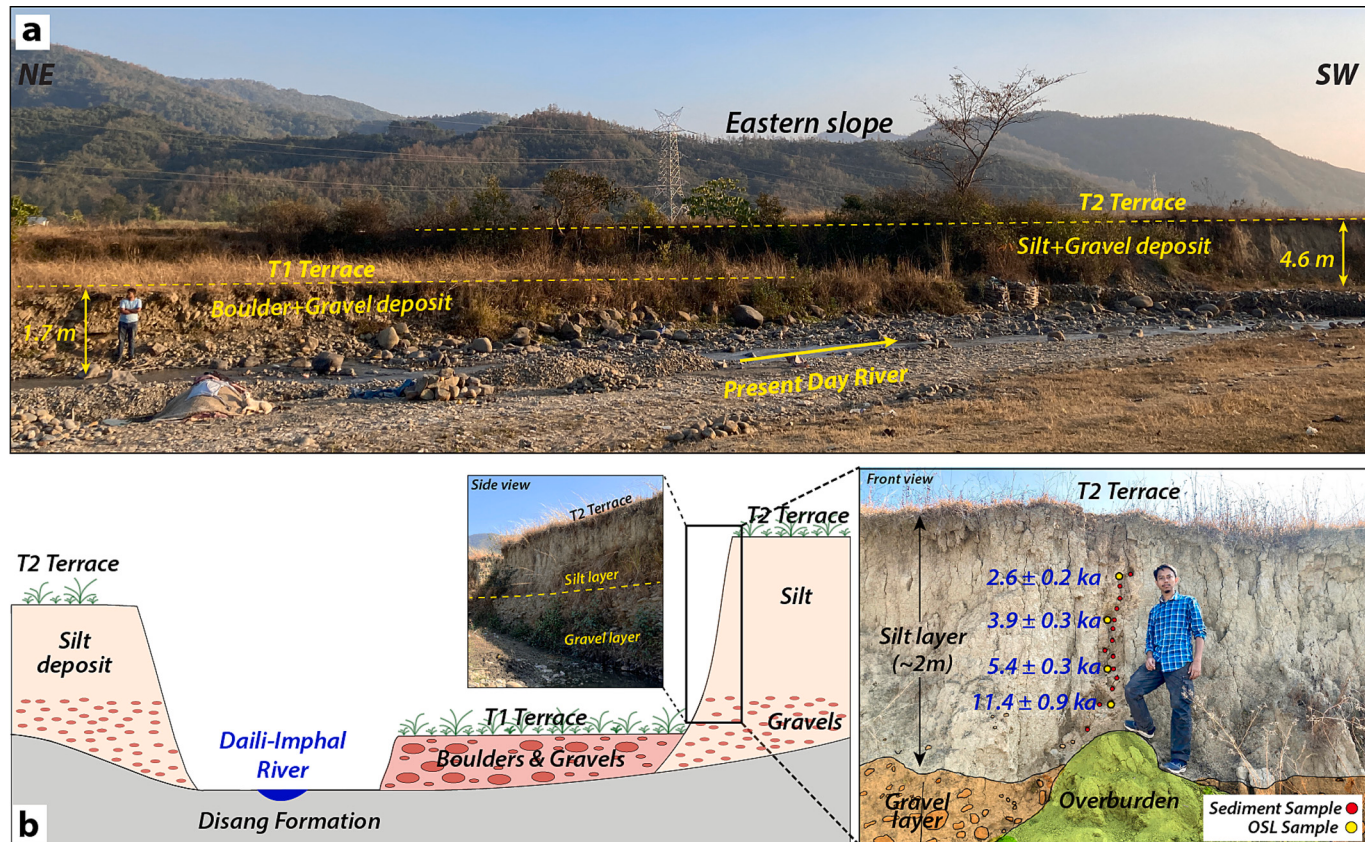


Fig. 4. (a) Well-developed T1 and T2 terraces along the Daili-Imphal River section (height of the person standing is 1.7 m). (b) Schematic section of the river terraces in the study area (not in scale), and Field photograph showing the vertical section of the T2 terrace. Yellow dots indicate OSL samples, and the red dots mark sample positions for grain-size and geochemical analyses at 10 cm intervals starting at 50 cm depth to 200 cm depth (height of the person is 1.6 m). (For interpretation of the references to colour in this figure legend, the reader is referred to the web version of this article.)

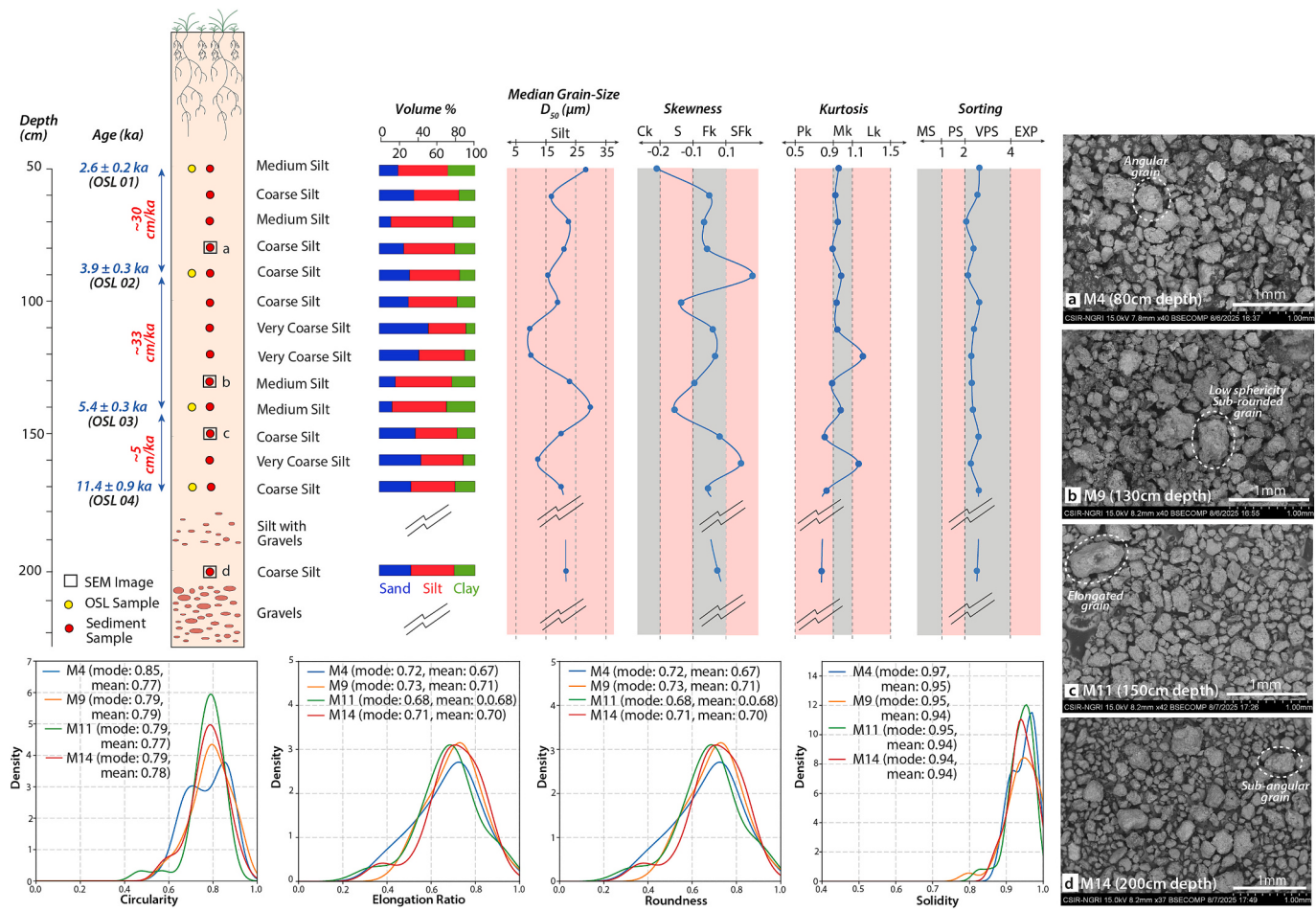


Fig. 5. The litho-log represents the depth Profile of the T2 terrace section with OSL ages and sedimentation rate, Particle size distribution in volume percentage, Median Grain Size (D_{50}), Kurtosis, Skewness, and Sorting of sediment samples (Pk- Platykurtic, Mk- Mesokurtic, Lk- Leptokurtic, Ck- Coarse skewed, S- Symmetric, Fk- Fine skewed, SFk-Strongly Fine skewed, MS-Medium Sorted, PS- Poorly Sorted, VPS- Very Poorly Sorted, EPS-Extremely Poorly Sorted). BSE-SEM photographs of sediment samples (a-d: M4, M9, M11, and M14) from depths 80, 130, 150, and 200 cm illustrate grain morphological characteristics. The distribution plots show the parameters C-Circularity, AR-Aspect Ratio, R-Roundness, and S-Solidity of the M4, M9, M11, and M14 samples.

characteristic of a lacustrine environment with minimal external disturbances (Folk and Ward, 1957).

Further, to understand the transportation process of the lacustrine deposit, which lacks laminae, we analyzed grain morphology. The samples M4, M9, M11, and M14 at 80, 130, 150, and 200 cm depth in the sediment column were analyzed under SEM. The BSE microphotographs of the corsair sediment fraction show that fine-medium grained sands are dominantly angular-subangular, low sphericity with sharp boundaries, and poor sorting (Fig. 5a-d). The medium to coarse sand grains (300–700 μm) were selected for grain morphology using an image analysis. The solidity values in the samples range between 0.88 and 1.00 in M4, 0.80–1.00 in M9, 0.82–0.98 in M11, and 0.87–0.92 in M14 (SM Table 1) with mean \pm standard deviation values of 0.95 ± 0.03 , 0.94 ± 0.04 , 0.94 ± 0.03 , and 0.94 ± 0.03 , respectively (Fig. 5). Circularitv values range between M4 = 0.58–0.89, M9 = 0.58–0.93, M11 = 0.47–0.88, and M14 = 0.57–0.92, with mean values of 0.77 ± 0.09 , 0.79 ± 0.09 , 0.77 ± 0.08 , and 0.78 ± 0.08 , respectively. The relatively low circularity values classify the grains as angular to sub-angular (Cox, 1927). Elongation ratio values range between M4 = 0.36–0.92, M9 = 0.46–0.98, M11 = 0.30–0.92, and M14 = 0.37–0.92, with corresponding means of 0.67 ± 0.14 , 0.71 ± 0.12 , 0.68 ± 0.14 , and 0.70 ± 0.13 ; suggesting slightly elongated grains (Blott and Pye, 2008). Roundness values, ranging between M4 = 0.36–0.92, M9 = 0.46–0.98, M11 = 0.30–0.92, and M14 = 0.37–0.92, with corresponding mean values of 0.67 ± 0.14 , 0.71 ± 0.12 , 0.68 ± 0.14 , and 0.70 ± 0.12 , respectively,

which categorize the grains as low-sphericity and sub-rounded (Powers, 1953). The overall distribution of these grain morphological parameters is unimodal and remains the same throughout the depths, suggesting no variation in the mode and energy of the transporting medium. The angular-subangular grains with low circularity and sphericity, slightly elongated and sub-rounded grains with poor sorting, homogeneity of grain size, and lack of sedimentary lamination in the sediment column (Fig. 5) point towards short transportation and piedmont-type deposition in the lacustrine depositional setting.

4.3. Geochemical signature of the sediment column

The Holocene lacustrine sediment column in the confined catchment of Daili-Imphal Valley shows little variability in the clay content, which is sensitive to chemical weathering. To understand the Holocene climatic variability and the provenance, we carried out the major-oxide analysis of 14 sediment samples collected at 10 cm intervals in the vertical section of the T2 terrace (Table 2). The oxides can be categorized into immobile and mobile categories based on their sensitivity to weathering. During weathering and sedimentary processes, Titanium (Ti) remains immobile, whereas Aluminum (Al) is relatively mobile but is still retained mainly in the solid phase, and silicon (Si) often leaches out. So, Al_2O_3 , MgO , TiO_2 , and SiO_2 are used as a proxy for detrital influx and hence used to measure rainfall and runoff from local watersheds (Wünnemann et al., 2010). The immobile oxide composition shows

Table 2

The major oxide data of the sediment samples (M1-M14) in the lake sediment column.

Major Oxides (%)	M1	M2	M3	M4	M5	M6	M7	M8	M9	M10	M11	M12	M13	M14
SiO ₂	63.89	63.85	63.35	62.98	65.77	64.56	63.74	62.84	64.81	64.77	64.14	63.93	66.6	64.31
Al ₂ O ₃	15.75	15.78	15.47	15.61	15.28	15.26	15.55	15.66	15.61	15.9	15.53	15.77	15.26	15.61
Fe ₂ O ₃	7.26	7.31	8.3	9.02	6.97	7.33	7.68	7.99	7.2	7.48	8.25	7.95	7.2	8.05
MnO	0.1	0.17	0.13	0.28	0.19	0.18	0.15	0.24	0.14	0.16	0.15	0.13	0.11	0.14
MgO	1.7	1.69	1.58	1.71	1.65	1.64	1.64	1.68	1.73	1.79	1.66	1.65	1.55	1.73
CaO	0.13	0.13	0.13	0.13	0.12	0.13	0.13	0.14	0.13	0.14	0.15	0.15	0.16	0.16
Na ₂ O	0.76	0.77	0.74	0.72	0.8	0.78	0.82	0.81	0.91	0.81	0.79	0.76	0.77	0.81
K ₂ O	2.32	2.26	2.2	2.2	2.08	2.14	2.25	2.28	2.23	2.24	2.28	2.29	2.05	2.31
TiO ₂	1.26	1.21	1.15	1.03	1.12	1.18	1.18	1.18	1.18	1.19	1.18	1.22	1.26	1.18
P ₂ O ₅	0.09	0.08	0.1	0.11	0.1	0.11	0.11	0.11	0.12	0.13	0.16	0.17	0.16	0.19
LOI	5.67	5.43	5.42	5.35	4.55	5.03	5.12	5.34	4.86	5.14	4.82	4.82	4.71	4.34
Sum	98.93	98.68	98.57	99.14	98.63	98.34	98.37	98.27	98.92	99.75	99.11	98.84	99.83	98.83

slight variation with SiO₂ ranging from 62 to 66 % and Al₂O₃ from 15.3 to 15.9 %, MgO from 1.5 to 1.8 % and TiO₂ from 1.1 to 1.3 % without any specific pattern in the sediment column (Table 2; Fig. 6a). Similarly, the mobile oxides concentration also remains uniform, such as Fe₂O₃ varies from 6.9 to 9.0 %, MnO from 0.3 to 1.0 %, CaO from 0.12 to 0.16 %, Na₂O from 0.7 to 0.9 %, and K₂O from 2.1 to 2.3 % in the sediment column. The Ti/Al and Si/Al ratios are commonly used alongside weathering indices to assess the degree of weathering, as it depends on climate influence and depositional environment (Bhushan et al., 2018). We observed very minute variations in the Ti/Al and Si/Al ratios, ranging between 0.07 and 0.09 and 3.5–4.0, respectively, without any

pattern in the sediment column (Fig. 6a).

Chemical Index of Alteration (CIA) measures the degree of chemical weathering in silicate rocks and is helpful in paleoclimatic reconstruction and provenance studies (Nesbitt and Young, 1982). The CIA values tend to be higher during warm and humid climates as mobile elements (K⁺, Ca²⁺, and Na⁺) tend to be removed, leading to relative enrichment of insoluble cations such as Al³⁺, and vice versa (Fedo et al., 1995; McLennan, 1993). Clastic sediments' compositional stability and maturity can be evaluated using the Index of Compositional Variability (ICV) (Cox et al., 1995), where a higher ICV value suggests low compositional maturity and less weathering in non-clay silicates. In

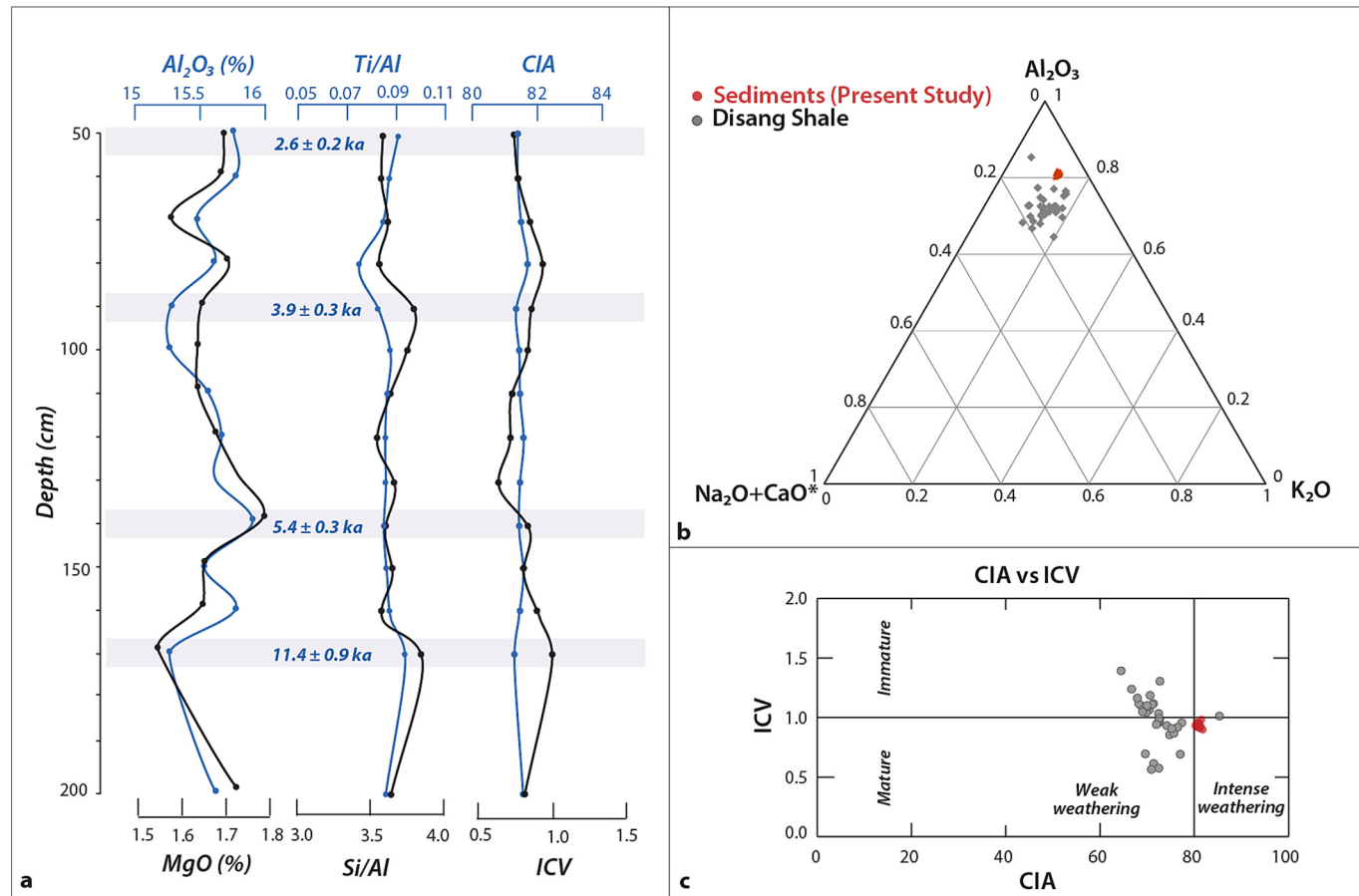


Fig. 6. (a) Depth profile of ICV, CIA, Al₂O₃, MgO, Ti/Al, and Si/Al ratio plots depicts the changes in the sediment chemistry; the shaded region indicates the age of the sediments derived from OSL dating. (b) A-CN-K ternary plot (Nesbitt and Young, 1982) showing composition of Disang shales and the fluvio-lacustrine sediments; (c) CIA vs. ICV plot of sediment samples in red colour (M1-M14) and Disang shales in grey colour (the major oxide data for Disang shale are taken from Majumdar and Chetia, 2011; Gogoi and Sarmah, 2013; SM Table 2). (For interpretation of the references to colour in this figure legend, the reader is referred to the web version of this article.)

contrast, a lower value indicates high weathering with abundant clay mineral growth and compositional maturity. We derived the CIA and ICV values using the major oxide composition of the sediments that range between 79 and 81 and 0.92–0.98 (Fig. 6a), respectively. The ICV vs. CIA plot (Long et al., 2012) reflects that the sediments did not alter much since deposition, as the values lie in the border zone of immature-mature and weak-intensely weathered categories (Fig. 6c).

To understand the sediment provenance and weathering history, we compared the geochemical signature of sediments (Table 2) with the bulk rock geochemistry of the Disang Shale (Majumdar and Chetia, 2011; Gogoi and Sarmah, 2013) (SM Table 2), which constitutes the bedrock in the Daili-Imphal valley (Fig. 1c). The average composition of Disang Shale and the lacustrine sediments in the A-CN-K ternary plot

(Fig. 6b) show a similar geochemical signature with slight depletion in the mobile $\text{CaO} + \text{Na}_2\text{O}$ and K_2O composition and enrichment of Al_2O_3 in the sediments (Fig. 6b). It suggests that the lake sediments underwent minimal chemical alteration during transportation and deposition. The ICV vs. CIA plot (Long et al., 2012) of the Disang Shale and the lacustrine sediments also suggests that the latter has experienced little weathering and chemical maturity (Fig. 6c). These changes in the lacustrine sediments indicate minimal transport from the source Disang Shale bedrock. However, no temporal changes in the weathering indices within the lacustrine sediments (Fig. 6b, c) indicated that Holocene climatic variability did not play any role in the chemical alteration process.

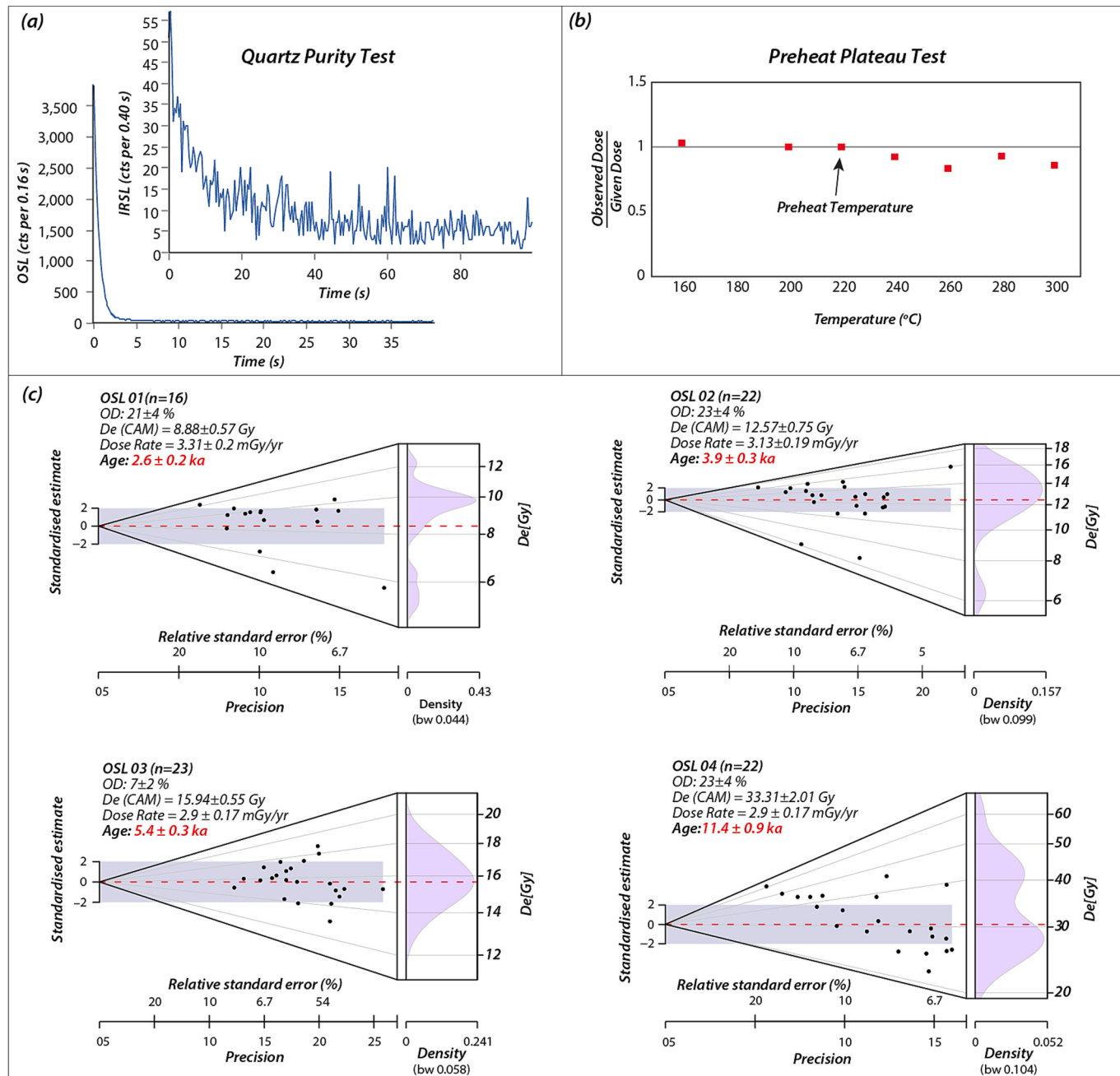


Fig. 7. (a) Decay curves showing the Infrared Stimulated Luminescence (IRSL) signal from feldspar grains and the Optically Stimulated Luminescence (OSL) signal from quartz grains obtained during the quartz purity test; (b) Result of the performed pre-heat plateau test; (c) Abanico plots showing De distribution of OSL samples (OSL 01–04), black dots represent an individual aliquot, and dashed red line indicates the central value (CAM) of equivalent dose (D_e) for each sample. (For interpretation of the references to colour in this figure legend, the reader is referred to the web version of this article.)

4.4. OSL dating of the sediment column

The suspended loads, originating from adjoining slopes composed of Disang Shale, were deposited in a small paleolake (Figs. 1a, 3a). The transportation of fine-grained sediments as suspended loads likely facilitated bleaching, ensuring reliable OSL age estimation. We carried out OSL dating of four samples (OSL 01–04) at depths of 50 cm, 90 cm, 140 cm, and 170 cm to uniformly cover the sediment column (Figs. 4, 5). The top 30–40 cm has well-developed humus affected by bioturbation, and the basal pebble beds were avoided for OSL dating. During the Quartz purity test on the samples, quartz OSL signal and k-feldspar IRSL signals show less than 5 % feldspar contribution, indicating the sample contains a datable quartz signal (Fig. 7a). The preheat plateau is attained at 220 °C, which is used as preheat temperature (Fig. 7b). The abanico

plots (Fig. 7c) (Dietze et al., 2016) show the Equivalent Dose (De) distribution of the OSL samples. Since the overdispersion is less than 23 %, ages were calculated using the Central Age Model (CAM) (Bailey and Arnold, 2006). The OSL samples yielded ages of 2.6 ± 0.23 ka, 3.9 ± 0.34 ka, 5.4 ± 0.38 ka, and 11.4 ± 0.97 ka at depths of 50 cm, 90 cm, 140 cm, and 170 cm, respectively (Table 1; Fig. 7c). The sedimentation rates were estimated by calculating the slope between the sampling distance and their successive deposition ages. The sedimentation rate varies from ~ 5 cm/ka between 140 and 170 cm to 33 cm/ka between 90 and 140 cm and 30 cm/ka between 50 and 90 cm depth (Figs. 5, 8, Table 1). The sedimentation rates between 50, 90, and 150 cm depths show a linear trend, and piecewise linear regression was used to approximate the sedimentation rate (Fig. 8). A slope of 32.17 cm/ka (~ 0.32 mm/yr) is obtained from this model ($R^2: 0.99$). It is assumed that

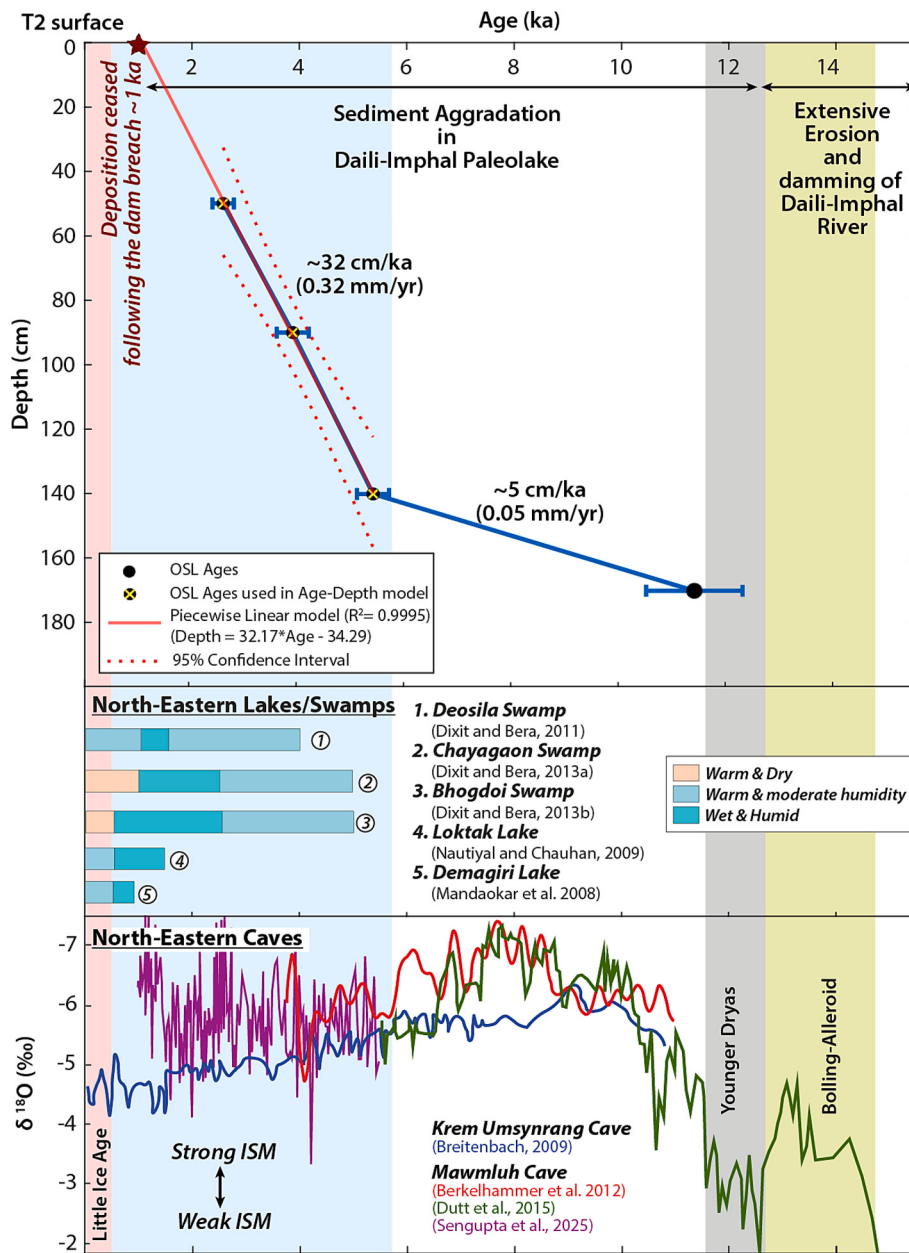


Fig. 8. Sedimentation rate in the Daili-Imphal lake plotted with the Late Quaternary-Holocene paleoclimatic proxies. The sedimentation rate was derived from the Age-Depth model and temporal comparison with paleoclimatic records of NE-Indian lakes/swamps and caves (red line is extrapolated to the T2 surface using the piecewise linear regression). The intersection of the extrapolated line (slope) with the zero-depth (top x-axis) of the T2 terrace surface represents the cessation of deposition by ~ 1 ka, before the dam breach. (For interpretation of the references to colour in this figure legend, the reader is referred to the web version of this article.)

sedimentation continued at this rate up to the top of the section, with the uppermost sediment estimated to be ~1 ka old (Fig. 8).

5. Discussion

The Late Pleistocene and Holocene global climate fluctuations drove geomorphic processes that are reflected in episodic dry and wet phases in lacustrine sediments across the Indian subcontinent (Rasmussen et al., 2006; Dutt et al., 2015; Misra et al., 2019; Brendryen et al., 2020; Bohra et al., 2024). The Trans-Himalayan high-altitude Tso-Kar Lake preserved the evidence of intensified summer monsoon during ~11.8 and 8.5–7 ka BP, followed by a mid-Holocene (~6–4 ka BP) weakened ISM and permafrost activity around 4.2 ka BP (Wünnemann et al., 2010). The intense wet ISM phases with distinct sedimentation characteristics were observed during ~11.5 ka, 11–10.5 ka, 10–9 ka, and 8–7 ka BP in the Malari landslide-dammed lake in the Higher Himalayas (Srivastava et al., 2013). The early Holocene high sedimentation rates tend to decrease during the mid-Holocene in the Benital Lake and Badani Tal in the Central Himalaya (Bhushan et al., 2018; Kotlia and Joshi, 2013). The early-to-mid-Holocene transition is also recorded in the playas and brackish-water lakes of western India, where ephemeral dry conditions with short wet spells between 6 and 5 ka BP and 5–3 ka BP followed increasing aridity (Enzel et al., 1999; Prasad et al., 1997).

In North-East India, the Holocene climatic fluctuations are well-recorded in the speleothem deposits in the Shillong Plateau caves (Breitenbach, 2009; Berkelhammer et al., 2012; Dutt et al., 2015; Sen-gupta et al., 2025), which lie adjacent to the study area (Figs. 1a, b, 8). The speleothems indicate a strengthened ISM between ~11–8 ka, stability from 8 to 6 ka, and a decline since ~6 ka (Fig. 8). However, the pollen records from the lakes/swamps in NE India (Fig. 1), having similar geomorphic setup as present study area, suggest persistence of warm and moderate humidity to wet and humid climate during the Mid-Late Holocene (Fig. 8; Mandaokar et al., 2008; Nautiyal and Chauhan, 2009; Dixit and Bera, 2011, 2013a, 2013b). The Holocene climatic fluctuations are preceded by a cold and dry period of Younger Dryas (YD) during 11.6–12.8 ka and a warm, humid period of Bølling-Allerød interstadial (B-A) during 12.8–14.6 ka (Rasmussen et al., 2006; Dutt et al., 2015; Brendryen et al., 2020; Fig. 8). The B-A event, which triggered significant ISM strengthening, is characterized by frequent storms, enhanced humidity, and extensive paleofloodings (Bohra et al., 2024).

5.1. Sedimentation vs. climatic variation

The Holocene climatic fluctuations caused noticeable changes in the erosion and sedimentation rate in the western Himalaya, Indo-Gangetic Plain, and other parts of the Indian subcontinent (Misra et al., 2019; Bohra et al., 2024). Lake sedimentation in the Daili-Imphal catchment began after the end of YD (Fig. 5) with the increasing strength of the ISM (Fig. 8). It is expected that the Daili-Imphal River catchment in NE India would have witnessed these climatic variabilities and would have reflected in the lacustrine deposit (Fig. 4) and associated landforms (Figs. 2, 3). We analyzed the lacustrine sediment column regarding geochemical proxies, grain size, and sedimentation rate variability (Figs. 4–7).

The sedimentary column shows minimal variation in the immobile and mobile components of the major oxides (Fig. 6; Table 1). The CIA and ICV indices, defining the weathering, have negligible variations throughout the Holocene (Fig. 6a), indicating the lacustrine sediments did not suffer climate-induced chemical weathering. However, the climatic fluctuations can be observed in the major oxide geochemistry and weathering indices in the Holocene sedimentary sequence across the Himalaya and western India (Kotlia and Joshi, 2013; Bali et al., 2016; Ngangom et al., 2017; Bhushan et al., 2018). The Daili-Imphal lacustrine sediments show a slight enrichment of immobile content in A-CN-K, CIA, and ICV plots compared to the Disang Shale with almost similar bulk geochemistry (Fig. 6b, c). This points towards the erosion of the source

Disang Shale and deposition of the sediments in the confined paleolake with a minuscule in-situ chemical alteration during the Late Pleistocene-Holocene.

Grain size variations in lake sediments may indicate hydrological energy, paleo-lake levels, distance from shoreline, and paleo-precipitation conditions (Håkanson and Jansson, 1983). The Holocene climatic variations are reflected in the grain-size variability of the paleolake sedimentary sequence (Nag et al., 2016; Ming et al., 2021). However, the grain size distribution in the Daili-Imphal lacustrine sediment column shows minor variation with median grain size (D_{50}) suggesting silt (15–25 μm) size particles throughout the Holocene (Fig. 5). The uniform median grain size (D_{50}) and fine skewness of the silt-sized sediments point towards a finer sediment source namely, the Disang Shale Formation, which forms the substrate in the catchment (Fig. 1c). The grain size reduction by long transportation would produce a good sorting in the sediment column, but the bulk sediment population is mesokurtic and poorly sorted (Fig. 5). The observed solidity index (Fig. 5) suggests that the sediments in the Daili-Imphal paleolake were transported primarily by fluvial processes, and the persistence of similar grain abrasion conditions throughout the sediment column (Fig. 5a-d) indicates stable hydrodynamic conditions (Gresina et al., 2023). The angular to sub-angular, slightly elongated, low sphericity, and sub-rounded to rounded grains (Fig. 5a-d) suggest either short to moderate transport distance or relatively high-energy but short-duration transport. When grains are transported over relatively long distances, abrasion of their edges increases roundness but does not modify their overall shape (Mazzullo and Magenheimer, 1987; Chmielowska et al., 2021); however, the distinct edges of subrounded grains are visible in the BSE images (Fig. 5a-d), supporting short-distance transport. This short transport could be the reason for negligible variations within the sediment column. Another factor that might have played a significant role is lithology, as the bedrock is composed of fine-grained shale and chemically matured rock. So, the effect of any climate-induced alteration in this short transport is negligible. The sediment column is largely massive, devoid of lamination, with poorly sorted sediments and subangular-subrounded and elongated grains (Figs. 4, 5), indicating deposition near the source zone without any marked variation in the basin hydrodynamics despite seasonal variability or Holocene climatic variability. This lack of transport and sediment characteristics points towards a local fine-grained source, namely the Disang shale Formation, and sediments were possibly derived from the adjoining western slopes, with deposition in the adjacent paleolake.

The lack of variation in the sedimentological character in the Holocene sediment column should be reflected in the sedimentation rate. However, the sedimentation rates derived from the Age-Depth model reveal that sediment aggradation throughout the Holocene is not uniform (Fig. 8). The sedimentation rate was ~0.05 mm/yr between 11.4 ka and 5.4 ka, which increases linearly to ~0.32 mm/yr between 5.4 ka to 2.6 ka and possibly continued until ~1 ka (Fig. 8). The observed Holocene sedimentation rate in Daili-Imphal paleolake is paradoxical as it is expected to have high sedimentation rate during strengthening phase of the ISM (~11–6 ka BP) and low during the weakening phase (~6 ka onward) as observed elsewhere (Srivastava et al., 2013; Bhushan et al., 2018; Bohra et al., 2024). The sedimentation rates in the paleolake records exhibit considerable variability in the different regions depending on the size of the catchment area, orographic control, lithology, and river discharge (Bohra et al., 2024). In the Central Himalaya, the Benital Lake experienced a higher sedimentation rate of 0.8–1.4 mm/yr during the early Holocene, which was reduced to 0.1 mm/yr during the mid and Late Holocene (Bhushan et al., 2018). In Malari Lake, the early Holocene shows ~1.2 mm/yr sedimentation rate but gradually decreased to 0.35 mm/yr during the mid-Holocene (Srivastava et al., 2013). Similarly, the Badani Tal experienced a sedimentation rate of 0.3–0.8 mm/yr during the Late Holocene (Kotlia and Joshi, 2013). However, the lakes in the Indo-Gangetic plain and Lonar Lake in Peninsular India show a similar paradox as they experienced a

lower sedimentation rate during the early and mid-Holocene, which increased abruptly during the Late Holocene (Prasad et al., 2014). The sedimentation rate of Sanai Tal was 0.04–0.07 mm/yr during the early and mid-Holocene, and it subsequently increased to 0.57 mm/yr during the Late Holocene (Sharma et al., 2006). The sedimentation in the Kerela Jheel was 0.1 mm/yr during the Early-Mid Holocene, and was later changed to 0.34 mm/yr during the Late Holocene (Chauhan et al., 2015). In Lashoda Lake, 0.09 mm/yr was observed during the Late Pliostocene to mid-Holocene, and changed to 0.8 mm/yr during the Mid-Late Holocene (Trivedi et al., 2019). During the Early-Mid Holocene, these lakes from the Indo-Gangetic Plain experienced a weakened southwest monsoon, prevailing less humid climate with low-energy fluvial conditions. These weakening phases of ISM could be the reason for the low sedimentation rate in the study area, as they can reduce the rate of sediment production by weathering. However, this low sedimentation rate during the Early Holocene period in the Daili-Imphal paleolake remains unexplained due to the lack of comparable archives in the other NE lakes and sedimentological characteristics (Figs. 1, 5, 6, 8). As pollen records suggested humid, warmer, and wetter climate prevailed during the Mid-Late Holocene in the northeastern region (Nautiyal and Chauhan., 2009; Mandaokar et al., 2008; Dixit and Bera, 2011, 2013a, 2013b), and Oxygen isotope study by Sengupta et al. (2025) from Mawmluh Cave is also showing prevalence of a stable climate with few episodes of intense ISM phases. This wet and humid climate might have enhanced the sediment production from the slopes and ultimately led to high sedimentation rates in the Daili-Imphal paleolake. Since NE India is a locus of higher precipitation, the paleoclimatic proxies are not very sensitive to the ISM strength variability; therefore, we explored the local geomorphic condition and surface processes (Figs. 3, 4) to understand the variations in the Holocene sedimentation pattern (Figs. 5, 7).

5.2. Geomorphic control on sedimentation

We have observed high erosion in the western slope of the Daili-Imphal catchment (Fig. 3) despite the study area being located in the topographically influenced rain-shadow zone (Fig. 1b). The GIS-based volumetric sediment budget estimation of the active CMF-affected western slope of the study area suggesting ~15 % of debris flow materials were preserved as piedmont fans; while the bulk of the regolith (85 %) were washed away (Fig. 3). The deformation due to CMF with a geodetic slip of 16 mm/yr (Gahalaut et al., 2013) may have also generated regolith during past seismic event(s). However, we did not observe any seismicites in the sediment column and are unsure of any seismic contribution in the Holocene catchment history. Despite the lack of long-term geological slip rate estimates, no paleoseismic studies have been reported for the study area. Minor micro-seismicity and earthquakes of 4–5 M were reported in the vicinity of CMF (Kumar et al., 2016), and the creep movement is affected by pore water pressure and shallow earthquake activity, causing slope failure (Kumar and Sanoujam, 2006).

We speculate that the short period of intense precipitation during the B-A event might have triggered extensive mass wasting on the upper slopes, and aggradation of Piedmont fans towards the lower slopes has subsequently dammed and blocked the narrow outlet of the Daili-Imphal catchment (Figs. 2, 3, 9a). The gravel-to-silt transition at the base of the T2 lacustrine deposit also points towards a strong surface runoff and debris flow-induced damming event before 11.4 ± 0.9 ka during the B-A phase (Figs. 8, 9). The cold and dry climate during YD (12.9–11.7 ka) would have stabilized the debris fan dam. The abrupt transition from basal gravel to thick silt deposit in the T2 suggests a sudden change in the hydrodynamics from extreme sediment-laden runoff to a deposition in a calm lacustrine environment (Lamoureux, 2002). The landslide-dammed lakes are the common ephemeral geomorphic features in active mountain regions whose stability depends on upstream channel

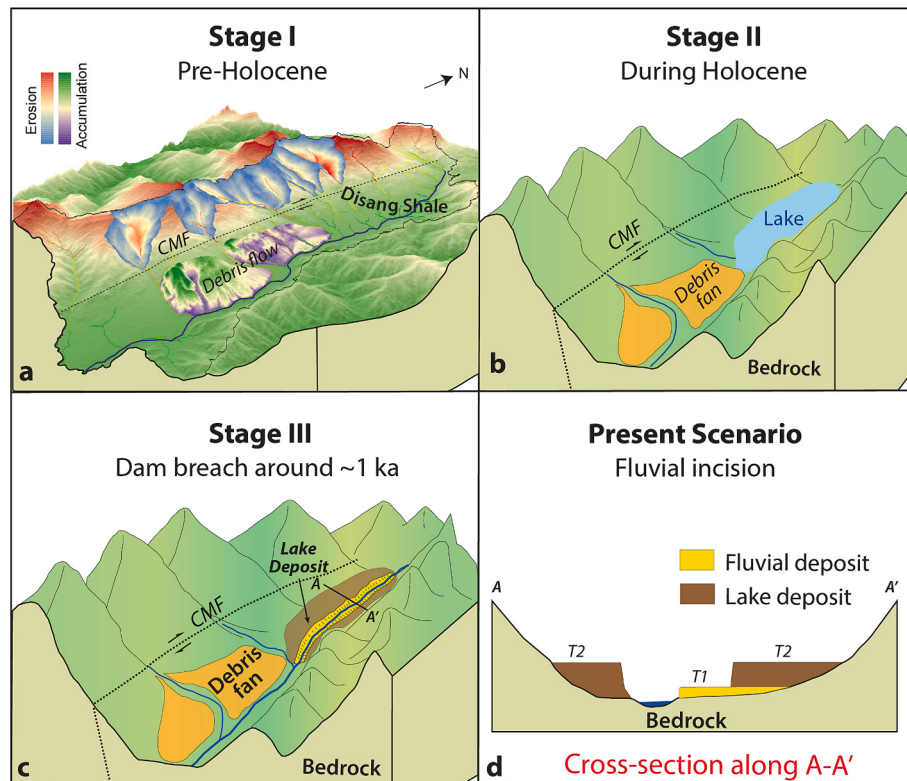


Fig. 9. Schematic representation showing stages of landscape evolution and terrace formation of the Daili-Imphal River. (a) Pre-Holocene stage-I shows the landscape before the river damming, possibly during Bølling-Allerød (B-A) interstadial during 12.8–14.6 ka. (b) Stage II represents Holocene sedimentation in the ephemeral paleolake. (c) Stage III represents the Dam breach at ~1 ka, (d) followed by incision and formation of terraces in the lacustrine deposit.

characteristics, tectonics, and climatic influences (Reneau and Dethier, 1996; Costa and Schuster, 1987; Guo et al., 2020). Since most regolith from the slopes was removed by extreme surface runoff during the B-A event, the sediment supply in the Daili-Imphal catchment remained limited during the early-mid Holocene (~11.5 ka) despite enhanced ISM strength (Figs. 8, 9b). However, prolonged exposure of the slope in the Daili-Imphal catchment to a humid and wet climate during the Mid-Late Holocene period (Nautiyal and Chauhan, 2009; Mandaokar et al., 2008; Dixit and Bera, 2011, 2013a, 2013b) would have caused high sediment production, resulting in a higher sedimentation rate (Fig. 8). This explains the counterintuitive low sedimentation rate during the Early-Mid Holocene, followed by a higher sedimentation rate during the Late Holocene. Extrapolating the sedimentation rate, it appears that the top of the T2 sedimentary column ceased deposition by ~1 ka in the Daili-Imphal paleolake (Fig. 8) and may represent the time of debris dam breach. The water withdrawal by the dam breach would have caused an incision into the lake deposit and formation of terraces, with the T2 terrace representing the Holocene lacustrine deposits of the Daili-Imphal paleolake. The lower T1 terrace represents the reworked basal deposits of the ephemeral paleolake, and the present Daili-Imphal river flows as a misfit channel with weak stream power during the past 1 ka over the substrate of Disang shale (Fig. 2), as marked by the very low k_{sn} (Fig. 3).

5.3. Coupling of climate variation, surface process, and sediment supply

It is globally observed that dam-forming landslides are invariably associated with mass wasting related to excessive precipitation and earthquakes in tectonically active regions (Costa and Schuster, 1987). Rock and debris avalanches, slumps, and slides are among the most common mass movements that form landslide dams. The study area in Daili-Imphal Valley lies adjacent to a tectonically active CMF undergoing ~16 mm/yr fault parallel geodetic deformation (Gahalaut et al., 2013; Fig. 1c). The CMF affected slope shows a distinct geomorphic characterization viz. the western fault block is experiencing erosion and debris fan growth in the eastern fault block (Fig. 3). We argue that the rain deficient Daili-Imphal valley has experienced extreme precipitation during Bølling-Allerød interstadial (B-A) (Dutt et al., 2015; Fig. 8), which caused extensive growth of debris dam and valley blockade (Fig. 9a). These types of mass-wasting-driven channel damming, producing ephemeral lakes, are commonly observed across active mountain belts (Hewitt, 1982; Dethier and Reneau, 1996; Costa and Schuster, 1987; Weidinger, 1998; Wang et al., 2019; Guo et al., 2020). Often, the stages of paleolake growth and episodic breach produce characteristic sediment variations (Hewitt, 1982; Dethier and Reneau, 1996; Costa and Schuster, 1987; Weidinger, 1998; Wang et al., 2019; Guo et al., 2020). However, the Holocene sedimentation in the Daili-Imphal paleolake remained homogeneous (Figs. 5, 6), though there was a marked change in the sedimentation rate post-Mid-Holocene climate transition (Kale, 2007). The paradoxical increase in sedimentation rate during the Mid-Late Holocene due to local climate fluctuation (Mandaokar et al., 2008; Nautiyal and Chauhan, 2009; Dixit and Bera, 2011, 2013a, 2013b) led to increased sediment influx (Fig. 8). This accumulation of the sediments would have reduced the capacity of the paleolake and produce an overflow, leading to the breach of the debris dam by <1 ka ago (Fig. 9c). Similar landslide lake breach is observed in the Argentina, Himalayas, Tibetan Plateau (Trauth and Strecker, 1999; Bookhagen et al., 2001; Wang et al., 2019). It is therefore important to analyze aspects of local tectono-geomorphic setup, surface processes, and climatic variation in exploring the Quaternary sediment archive as they undergo complex interaction in tectonically active areas.

6. Conclusion

The intermontane Daili-Imphal valley in the Indo-Burmese Range experienced a channel blockade and development of a paleolake, which experienced continuous sedimentation during the Holocene (11.4 ± 0.9

ka to $<2.6 \pm 0.2$ ka). The transient landscape modeling, erosional volume estimate, detailed sedimentological and geochemical studies on the lake sediments suggest that the silt-dominant sediments were derived from adjoining regions and deposited without any marked hydrodynamic fluctuation in the paleolakes, as marked by the lack of noticeable grain-size variation and development of bedding/lamination in the sediment column. The sediment chemistry points towards the Disang Shale source, and the lack of variations in the sediment column suggests minimal chemical weathering during the Holocene climate fluctuations. However, OSL chronology indicates a paradoxically low sedimentation rate during the Early Holocene and high during the Mid-Late Holocene when climate vigor is ebbing. The other paleoclimatic studies suggested a local humid-warm climate during the Mid-Late Holocene, which might be responsible for increased sedimentation rates. Further comparing the erosional and aggradational landscape suggests that ~15 % of the total mass wasting from the adjoining slopes is preserved in debris fans, which block the Daili-Imphal valley. We argue that the pre-Holocene Bølling-Allerød climatic maxima caused excessive mass wasting, blocking the river with debris fans and depriving the sediment supply slopes during the Early Holocene. This unique geomorphic and local climatic variation control is important in exploring the Quaternary sediment archive, which deepens our understanding of the interplay between climate and surface processes. These findings also illuminate a complex interaction of the fluvial landscape evolution and erosion-aggradation patterns in a fluctuating climatic setup.

CRediT authorship contribution statement

Arindom Gogoi: Writing – original draft, Visualization, Methodology, Investigation, Formal analysis, Data curation, Conceptualization. **Prabha Pandey:** Writing – review & editing, Writing – original draft, Supervision, Funding acquisition, Conceptualization. **Anand K. Pandey:** Writing – review & editing, Writing – original draft, Visualization, Supervision, Funding acquisition, Conceptualization.

Declaration of competing interest

The authors declare that they have no conflict of interest.

Acknowledgments

We highly appreciate detailed comments and suggestions by anonymous reviewers, which clarified the manuscript. The Director, CSIR-NGRI, is acknowledged for providing the facilities, fund MLP-7014-28 (AKP), and permission to publish (NGRI/Lib/2025/Pub-84). The work is a part of AG's Ph.D. research, with support of a University Grants Commission Fellowship (grant no. 191620014229). We thank Raghuvir Konduru for assistance in the field and OSL dating.

Appendix A. Supplementary data

Supplementary data to this article can be found online at <https://doi.org/10.1016/j.palaeo.2025.113279>.

Data availability

The authors confirm that all data necessary for supporting the scientific findings of this paper have been provided.

References

- Acharya, S.K., 2010. Tectonic evolution of Indo-Burma Range with special reference to Naga-Manipur Hills. *Mem. Geol. Soc. Ind.* 75, 25–43.
- Aitken, M.J., 1998. An introduction to optical dating: the dating of Quaternary sediments by the use of photon-stimulated luminescence. *Choice Rev. Online* 36 (11), 36–6294. <https://doi.org/10.5860/choice.36-6294>.

- Allen, J.R.L., 1985. Principles of physical sedimentology. In: Springer eBooks. <https://doi.org/10.1007/978-94-010-9683-6>.

Allen, J.R., Thornley, D.M., 2004. Laser granulometry of Holocene estuarine silts: effects of hydrogen peroxide treatment. *Holocene* 14 (2), 290–295. <https://doi.org/10.1191/095963604hl681rr>.

Bailey, R., Arnold, L., 2006. Statistical modelling of single grain quartz De distributions and an assessment of procedures for estimating burial dose. *Q. Sci. Rev.* 25 (19–20), 2475–2502. <https://doi.org/10.1016/j.quascirev.2005.09.012>.

Bali, R., Khan, I., Sangode, S., Mishra, A.K., Ali, S.N., Singh, S.K., Tripathi, J.K., Singh, D.S., Srivastava, P., 2016. Mid-to-late Holocene climate response from the Triloknath palaeolake, Lahaul Himalaya, based on multiproxy data. *Geomorphology* 284, 206–219. <https://doi.org/10.1016/j.geomorph.2016.10.028>.

Barrett, P.J., 1980. The shape of rock particles, a critical review. *Sedimentology* 27 (3), 291–303. <https://doi.org/10.1111/j.1365-3091.1980.tb01179.x>.

Berkelhammer, M., Sinha, A., Stott, L., Cheng, H., Pausata, F., Yoshimura, K., 2012. An abrupt shift in the Indian monsoon 4000 years ago. In: *Geophysical Monograph*, pp. 75–88. <https://doi.org/10.1029/2012gm001207>.

Beuselinck, L., Govers, G., Poesen, J., Degraer, G., Froyen, L., 1998. Grain-size analysis by laser diffractometry: comparison with the sieve-pipette method. *CATENA* 32 (3–4), 193–208. [https://doi.org/10.1016/s0341-8162\(98\)00051-4](https://doi.org/10.1016/s0341-8162(98)00051-4).

Bhushan, R., Sati, S., Rana, N., Shukla, A., Mazumdar, A., Juyal, N., 2018. High-resolution millennial and centennial scale Holocene monsoon variability in the higher Central Himalayas. *Palaeogeogr. Palaeoclimatol. Palaeoecol.* 489, 95–104. <https://doi.org/10.1016/j.palaeo.2017.09.032>.

Blott, S.J., Pye, K., 2001. GRADISTAT: a grain size distribution and statistics package for the analysis of unconsolidated sediments. *Earth Surf. Process. Landf.* 26 (11), 1237–1248. <https://doi.org/10.1002/esp.261>.

Blott, S.J., Pye, K., 2008. Particle shape: a review and new methods of characterization and classification. *Sedimentology* 55 (1), 31–63. <https://doi.org/10.1111/j.1365-3091.2007.00892.x>.

Booga, S., 2009. *Petrology of Sedimentary Rocks*. Cambridge University Press.

Bohra, A., Laskar, A.H., Mehta, M., Anoop, A., Pandey, A.K., 2024. Late Quaternary palaeoclimatic records from the Indian Himalaya and Ganga foreland basin: assessment on current understanding and future prospective. *Q. Sci. Adv.* 13, 100152. <https://doi.org/10.1016/j.qsa.2023.100152>.

Bookhagen, B., Burbank, D.W., 2010. Toward a complete Himalayan hydrological budget: Spatiotemporal distribution of snowmelt and rainfall and their impact on river discharge. *J. Geophys. Res. Atmos.* 115 (F3). <https://doi.org/10.1029/2009jf001426>.

Bookhagen, B., Haselton, K., Trauth, M.H., 2001. Hydrological modelling of a Pleistocene landslide-dammed lake in the Santa María Basin, NW Argentina. *Palaeogeogr. Palaeoclimatol. Palaeoecol.* 169 (1–2), 113–127. [https://doi.org/10.1016/s0031-0182\(01\)00221-8](https://doi.org/10.1016/s0031-0182(01)00221-8).

Breitenbach, S., 2009. Changes in Monsoonal Precipitation and Atmospheric Circulation During the Holocene Reconstructed from Stalagmites from Northeastern India. Doctoral dissertation, Potsdam University. Institutional Repository of the University of Potsdam. <http://opus.kobv.de/ubp/volltexte/2009/3780/>.

Brendryen, J., Haflidason, H., Yokoyama, Y., Haaga, K.A., Hannisdal, B., 2020. Eurasian Ice Sheet collapse was a major source of Meltwater Pulse 1A 14,600 years ago. *Nat. Geosci.* 13 (5), 363–368. <https://doi.org/10.1038/s41561-020-0567-4>.

Chauhan, M.S., Pokharkar, A.K., Srivastava, R.K., 2015. Late Quaternary vegetation history, climatic variability and human activity in the Central Ganga Plain, deduced by pollen proxy records from Karella Jheel, India. *Quat. Int.* 371, 144–156. <https://doi.org/10.1016/j.quaint.2015.03.025>.

Chmielowska, D., Woronko, B., Doroski, S., 2021. Applicability of automatic image analysis in quartz-grain shape discrimination for sedimentary setting reconstruction. *CATENA* 207, 105602. <https://doi.org/10.1016/j.catena.2021.105602>.

Costa, J.E., Schuster, R.L., 1987. The formation and failure of natural dams. In: USGS Open-File Report 87-392. <https://doi.org/10.3133/ofr87392>.

Cox, E.P., 1927. A method of assigning numerical and percentage values to the degree of roundness of sand grains. *J. Paleo.* 1 (3), 179–183. <https://pubs.geoscienceworld.org/jpaleont/article/1/3/179/77577/A-method-of-assigning-numerical-and-perce-nce>.

Cox, R., Lowe, D.R., Cullers, R., 1995. The influence of sediment recycling and basement composition on evolution of mudrock chemistry in the southwestern United States. *Geochim. Cosmochim. Acta* 59 (14), 2919–2940. [https://doi.org/10.1016/0016-7037\(95\)00185-9](https://doi.org/10.1016/0016-7037(95)00185-9).

Dethier, D.P., Renau, S.L., 1996. Lacustrine chronology links late Pleistocene climate change and mass movements in northern New Mexico. *Geology* 24 (6), 539. [https://doi.org/10.1130/0091-7613\(1996\)024a.1.0.co;2](https://doi.org/10.1130/0091-7613(1996)024a.1.0.co;2).

Dietze, M., Kreutzer, S., Burow, C., Fuchs, M.C., Fischer, M., Schmidt, C., 2016. The abanico plot: Visualising chronometric data with individual standard errors. *Quat. Geochronol.* 31, 12–18. <https://doi.org/10.1016/j.quageo.2015.09.003>.

Dixit, S., Bera, S.K., 2011. Mid-Holocene vegetation and climatic variability in tropical deciduous Sal (*Shorea robusta*) forest of lower Brahmaputra valley, Assam. *J. Geol. Soc. India* 77 (5), 419–432. <https://doi.org/10.1007/s12594-011-0051-2>.

Dixit, S., Bera, S., 2013a. Pollen-inferred vegetation Vis-à-vis climate dynamics since late Quaternary from western Assam, Northeast India: Signal of global climatic events. *Quat. Int.* 286, 56–68. <https://doi.org/10.1016/j.quaint.2012.06.010>.

Dixit, S., Bera, S., 2013b. Vegetation vis-à-vis climate change around Bhogdoi swamp in lower Brahmaputra flood plain of Assam, Northeast India since Late Holocene. *J. Palaeosci.* 62 (1–2), 19–27. <https://doi.org/10.5499/jop.2013.332>.

Dutt, S., Gupta, A.K., Clemens, S.C., Cheng, H., Singh, R.K., Kathayat, G., Edwards, R.L., 2015. Abrupt changes in Indian summer monsoon strength during 33,800 to 5500 years BP. *Geophys. Res. Lett.* 42 (13), 5526–5532.

Enzel, Y., Ely, L.L., Mishra, S., Ramesh, R., Amit, R., Lazar, B., Rajaguru, S.N., Baker, V.R., Sandler, A., 1999. High-Resolution Holocene environmental changes in the Thar Desert, northwestern India. *Science* 284 (5411), 125–128. <https://doi.org/10.1126/science.284.5411.125>.

Evans, P., 1932. Tertiary succession in Assam. *Trans. Min. Geol. Inst. India* 27 (3), 155–260.

Fedo, C.M., Nesbitt, H.W., Young, G.M., 1995. Unraveling the effects of potassium metasomatism in sedimentary rocks and paleosols, with implications for paleoweathering conditions and provenance. *Geology* 23 (10), 921. [https://doi.org/10.1130/0091-7613\(1995\)023a.1.0.co;2](https://doi.org/10.1130/0091-7613(1995)023a.1.0.co;2).

Folk, R.L., Ward, W.C., 1957. Brazos River bar [Texas]; a study in the significance of grain size parameters. *J. Sediment. Res.* 27 (1), 3–26. <https://doi.org/10.1306/74d06462b211d7-8648000102c1865d>.

Gahalaut, V.K., Kundu, B., Laishram, S.S., Catherine, J., Kumar, A., Singh, M.D., Tiwari, R.P., Chadha, R.K., Samanta, S.K., Ambikapathy, A., Mahesh, P., Bansal, A., Narasiah, M., 2013. Aseismic plate boundary in the Indo-Burman wedge, Northwest Sunda Arc. *Geology* 41 (2), 235–238. <https://doi.org/10.1130/g33771.1>.

Gogoi, B.K., Sarmah, R.K., 2013. Geochemical Characteristics of Shale of Disang Group, Tirap District, Arunachal Pradesh. *Int. J. Sci. Technol. Res.* 2 (11), 186–192.

Gresina, F., Farkas, B., Fábián, S.Á., Szalai, Z., Varga, G., 2023. Morphological analysis of mineral grains from different sedimentary environments using automated static image analysis. *Sediment. Geol.* 455, 106479. <https://doi.org/10.1016/j.sedgeo.2023.106479>.

Guo, C., Montgomery, D.R., Zhang, Y., Zhong, N., Fan, C., Wu, R., Yang, Z., Ding, Y., Jin, J., Yan, Y., 2020. Evidence for repeated failure of the Yigong landslide on the edge of the Tibetan Plateau. *Sci. Rep.* 10 (1). <https://doi.org/10.1038/s41598-020-71335-w>.

Hewitt, K., 1982. Natural dams and outburst floods of the Karakoram Himalaya. In: *Hydrological Aspects of Alpine and High Mountain Areas (Proceedings of the Exeter Symposium-1982)*. IAHS Publ. no. 138, pp. 259–269.

Kale, V.S., 2007. Fluvio-sedimentary response of the monsoon-fed Indian rivers to Late Pleistocene-Holocene changes in monsoon strength: reconstruction based on existing 14C dates. *Quat. Sci. Rev.* 26 (11–12), 1610–1620. <https://doi.org/10.1016/j.quascirev.2007.03.012>.

Kotlia, B.S., Joshi, L.M., 2013. Late Holocene climatic changes in Garhwal Himalaya. *Curr. Sci.* 104 (7), 911–919. <http://www.jstor.org/stable/24092104>.

Kumar, A., Sanoujam, M., 2006. Landslide studies along the national highway (NH 39) in Manipur. *Nat. Hazards* 40 (3), 603–614. <https://doi.org/10.1007/s11069-006-9024-y>.

Kumar, A., Sanoujam, M., Someshwar Roy, L., Kosigyn, L., Arun Kumar Singh, W., Pandey, A.P., 2016. Mw 6.7 earthquake of Manipur, NE India: Some Insights. *Jour. Geol. Soc. India* 88 (1), 5–12. <https://doi.org/10.1007/s12594-016-0452-3>.

Lamoureux, S., 2002. Temporal patterns of suspended sediment yield following moderate to extreme hydrological events recorded in varved lacustrine sediments. *Earth Surf. Process. Landf.* 27 (10), 1107–1124. <https://doi.org/10.1002/esp.399>.

Liang, P., Forman, S.L., 2019. LDAC: an Excel-based program for luminescence equivalent dose and burial age calculations. *Ancient TL* 37 (2), 21–40. <https://doi.org/10.26034/la.atl.2019.536>.

Long, X., Yuan, C., Sun, M., Xiao, W., Wang, Y., Cai, K., Jiang, Y., 2012. Geochemistry and Nd isotopic composition of the early Paleozoic flysch sequence in the Chinese Altai, Central Asia: evidence for a northward derived mafic source and insight into Nd model ages in accretionary orogen. *Gondw. Res.* 22, 554–566.

Majumdar, D., Chetia, B.K., 2011. Role of geochemistry of the Disang Shales in the interpretation of their depositional environment. In: *Proc. of the 17th Conv. of Ind. Geol. Cong. And Int. Conf. NPESMD*, pp. 299–311.

Mandaokar, B., Chauhan, Chatterjee, S., 2008. Fungal remains from the late Holocene lake deposit of Demagiri, Mizoram, India and their palaeoclimatic implications. *J. Palaeontol. Soc. India* 53 (2), 197–205. <https://doi.org/10.1177/0971102320080208>.

Mazzullo, J., Magenheimer, S., 1987. The original shapes of quartz sand grains. *J. Sediment. Res.* 57. <https://doi.org/10.1306/212f8b6-2b24-11d7-8648000102c1865d>.

McLennan, S.M., 1993. Weathering and global denudation. *J. Geol.* 101 (2), 295–303. <http://www.jstor.org/stable/30081153>.

Ming, G., Zhou, W., Wang, H., Shu, P., Cheng, P., Liu, T., Zhou, J., 2021. Grain size variation in two lakes from margin of Asian Summer Monsoon and its paleoclimate implications. *Palaeogeogr. Palaeoclimatol. Palaeoecol.* 567, 110295. <https://doi.org/10.1016/j.palaeo.2021.110295>.

Misra, P., Tandon, S., Sinha, R., 2019. Holocene climate records from lake sediments in India: Assessment of coherence across climate zones. *Earth Sci. Rev.* 190, 370–397. <https://doi.org/10.1016/j.earscirev.2018.12.017>.

Mitra, R.N., 1971. Tectonics of the frontal folded belt of Tripura-Surma Valley. *Bull. Oil Nat. Gas. Comm.* 8 (2), 71–75.

Murray, A., Arnold, L.J., Buylaert, J., Guérin, G., Qin, J., Singhvi, A.K., Smedley, R., Thomsen, K.J., 2021. Optically stimulated luminescence dating using quartz. *Nat. Rev. Methods Prim.* 1 (1). <https://doi.org/10.1038/s43586-021-00068-5>.

Nag, D., Phartiyal, B., Singh, D.S., 2016. Sedimentary characteristics of palaeolake deposits along the Indus River valley, Ladakh, Trans-Himalaya: Implications for the depositional environment. *Sedimentology* 63 (6), 1765–1785. <https://doi.org/10.1111/sed.12289>.

Nandy, D.R., 1986. Geology and tectonics of Arakan Yoma - a reappraisal. *Bull. Geol. Soc. of Malaysia* 20, 137–148. <https://doi.org/10.7186/bgsm20198608>.

Nautiyal, C., Chauhan, , 2009. Late Holocene vegetation and climate change in Loktak Lake region, Manipur, based on pollen and chemical evidence. *J. Palaeosci.* 58 (1–3), 21–28. <https://doi.org/10.5499/jop.2009.78>.

- Nesbitt, H.W., Young, G.M., 1982. Early Proterozoic climates and plate motions inferred from major element chemistry of lutites. *Nature* 299 (5885), 715–717. <https://doi.org/10.1038/299715a0>.
- Ngangom, M., Bhandari, S., Thakkar, M., Shukla, A.D., Juyal, N., 2017. Mid-Holocene extreme hydrological events in the eastern Great Rann of Kachchh, western India. *Quat. Int.* 443, 188–199. <https://doi.org/10.1016/j.quaint.2016.10.017>.
- Panda, D., Kundu, B., Gahalaut, V.K., Rangin, C., 2020. India-Sunda plate motion, crustal deformation, and seismic hazard in the Indo-Burmese arc. *Tectonics* 39 (8). <https://doi.org/10.1029/2019tc006034>.
- Pandey, P., Kumar, R., Suresh, N., Sangode, S.J., Pandey, A.K., 2009. Soft-Sediment deformation in contemporary reservoir sediment: A repository of recent major earthquake events in Garhwal Himalaya. *J. Geol.* 117 (2), 200–209. <https://doi.org/10.1086/595860>.
- Pandey, A.K., Pandey, P., Singh, G.D., Juyal, N., 2014. Climate footprints in the late Quaternary-Holocene landforms of Dun Valley, NW Himalaya, India. *Curr. Sci.* 106 (2), 245–253. <https://doi.org/10.18520/cs/v106/i2/245-253>.
- Pettit, J.R., Jouzel, J., Raynaud, D., Barkov, N.I., Barnola, J., Basile, I., Bender, M., Chappellaz, J., Davis, M., Delaygue, G., Delmotte, M., Kotlyakov, V.M., Legrand, M., Lipenkov, V.Y., Lorius, C., Pépin, L., Ritz, C., Saltzman, E., Steenbard, M., 1999. Climate and atmospheric history of the past 420,000 years from the Vostok ice core, Antarctica. *Nature* 399 (6735), 429–436. <https://doi.org/10.1038/20859>.
- Powers, N.M.C., 1953. A new roundness scale for sedimentary particles. *J. Sediment. Res.* 23. <https://doi.org/10.1306/d4269567-2b26-11d7-8648000102c1865d>.
- Prasad, S., Kusumgar, S., Gupta, S.K., 1997. A mid to late Holocene record of palaeoclimatic changes from Nal Sarovar: a palaeodesert margin lake in western India. *J. Quat. Sci.* 12 (2), 153–159. [https://doi.org/10.1002/\(sici\)1099-1417\(199703/04\)12:2](https://doi.org/10.1002/(sici)1099-1417(199703/04)12:2).
- Prasad, S., Anoop, A., Riedel, N., Sarkar, S., Menzel, P., Basavaiah, N., Krishnan, R., Fuller, D., Plessen, B., Gaye, B., Röhl, U., Wilkes, H., Sachse, D., Sawant, R., Wiesner, M., Stebich, M., 2014. Prolonged monsoon droughts and links to Indo-Pacific warm pool: A Holocene record from Lonar Lake, Central India. *Earth Planet. Sci. Lett.* 391, 171–182. <https://doi.org/10.1016/j.epsl.2014.01.043>.
- Rasmussen, S.O., Andersen, K.K., Svensson, A.M., Steffensen, J.P., Vinther, B.M., Clausen, H.B., Siggaard-Andersen, M., Johnsen, S.J., Larsen, L.B., Dahl-Jensen, D., Bigler, M., Röhlisberger, R., Fischer, H., Goto-Azuma, K., Hansson, M.E., Ruth, U., 2006. A new Greenland ice core chronology for the last glacial termination. *J. Geophys. Res. Atmos.* 111 (D6). <https://doi.org/10.1029/2005jd006079>.
- Reneau, S.L., Dethier, D.P., 1996. Late Pleistocene landslide-dammed lakes along the Rio Grande, White Rock Canyon, New Mexico. *Geol. Soc. Am. Bull.* 108 (11), 1492–1507. [https://doi.org/10.1130/0016-7606\(1996\)108.1-7.https://doi.org/10.5194/esurf-2-1-2014](https://doi.org/10.1130/0016-7606(1996)108.1-7.https://doi.org/10.5194/esurf-2-1-2014).
- Sengupta, D., Dutt, S., Warken, S.F., Singam, A., Frank, N., Sagwal, S., Maurya, S., 2025. Climate-change-induced human migration and socio-political changes in eastern India during the Meghalayan age. *Palaeogeogr. Palaeoclimatol. Palaeoecol.* 112873 <https://doi.org/10.1016/j.palaeo.2025.112873>.
- Sharma, S., Joachimski, M.M., Tobschall, H.J., Singh, I.B., Sharma, C., Chauhan, M.S., 2006. Correlative evidences of monsoon variability, vegetation change and human inhabitation in Sanai lake deposit: Ganga Plain, India. *Curr. Sci.* 90, 973–978.
- Small, E.E., Anderson, R.S., 1998. Pleistocene relief production in Laramide mountain ranges, western United States. *Geology* 26 (2), 123. [https://doi.org/10.1130/0091-7613\(1998\)026](https://doi.org/10.1130/0091-7613(1998)026).
- Srivastava, P., Kumar, A., Mishra, A., Meena, N.K., Tripathi, J.K., Sundriyal, Y., Agnihotri, R., Gupta, A.K., 2013. Early Holocene monsoonal fluctuations in the Garhwal higher Himalaya as inferred from multi-proxy data from the Malari paleolake. *Quatern. Res.* 80 (3), 447–458. <https://doi.org/10.1016/j.yqres.2013.07.006>.
- Trauth, M.H., Strecker, M.R., 1999. Formation of landslide-dammed lakes during a wet period between 40,000 and 25,000 yr BP in northwestern Argentina. *Palaeogeogr. Palaeoclimatol. Palaeoecol.* 153 (1–4), 277–287. [https://doi.org/10.1016/s0031-0182\(99\)00078-4](https://doi.org/10.1016/s0031-0182(99)00078-4).
- Trivedi, A., Saxena, A., Chauhan, Sharma, A., Farooqui, A., Nautiyal, C., Yao, Y., Wang, Y., Li, C., & Tiwari, D., 2019. Vegetation, climate and culture in Central Ganga plain, India: A multi-proxy record for last Glacial Maximum. *Quat. Int.* 507, 134–147. <https://doi.org/10.1016/j.quaint.2019.02.019>.
- Wadell, H., 1932. Volume, shape, and roundness of rock particles. *J. Geol.* 40 (5), 443–451. <https://doi.org/10.1086/623964>.
- Wang, H., Cui, P., Liu, D., Liu, W., Bazai, N.A., Wang, J., Zhang, G., Lei, Y., 2019. Evolution of a landslide-dammed lake on the southeastern Tibetan Plateau and its influence on river longitudinal profiles. *Geomorphology* 343, 15–32. <https://doi.org/10.1016/j.geomorph.2019.06.023>.
- Weidinger, J.T., 1998. Case history and hazard analysis of two lake-damming landslides in the Himalayas. *J. Asian Earth Sci.* 16 (2–3), 323–331. [https://doi.org/10.1016/s0743-9547\(98\)00026-9](https://doi.org/10.1016/s0743-9547(98)00026-9).
- Whipple, K.X., Tucker, G.E., 1999. Dynamics of the stream-power river incision model: Implications for height limits of mountain ranges, landscape response timescales, and research needs. *J. Geophys. Res. Atmos.* 104 (B8), 17661–17674. <https://doi.org/10.1029/1999jb900120>.
- Wobus, C., Whipple, K.X., Kirby, E., Snyder, N., Johnson, J., Spyropoulos, K., Crosby, B., Sheehan, D., 2006. Tectonics from topography: procedures, promise, and pitfalls. In: Geological Society of America eBooks. [https://doi.org/10.1130/2006.2398\(04](https://doi.org/10.1130/2006.2398(04).
- Wünnemann, B., Demsk, D., Tarasov, P., Kotlia, B.S., Reinhardt, C., Bloemendal, J., Diekmann, B., Hartmann, K., Krois, J., Riedel, F., 2010. Hydrological evolution during the last 15kyr in the Tso Kar lake basin (Ladakh, India), derived from geomorphological, sedimentological and palynological records. *Q. Sci. Rev.* 29 (9–10), 1138–1155. <https://doi.org/10.1016/j.quascirev.2010.02.017>.
- Håkanson, L., Jansson, M., 1983. Principles of lake sedimentology. Springer eBooks. <https://doi.org/10.1007/978-3-642-69274-1>.